Master Thesis Submitted as Partial Fulfilment
of the Requirements for the Degree of
M.Sc. Environmental Physics

Quantification of basal Glacial Meltwater from the Filchner-Ronne Ice Shelf using time series of noble gases

Author
Hendrik Jechlitschek

Supervisor and 1st Reviewer
Dr. Oliver Huhn
Institute for Environmental Physics
Oceanography Department

2nd Reviewer
Dr. Christian Melsheimer
Institute for Environmental Physics
Remote Sensing of Sea Ice

Submitted
Bremen, 12.09.2024

This is version of the was modified for the purpose of uploading it to the IUP Bremen homepage. The adjustments made are for display reasons only. No changes to the content were made. Bremen, 19.01.2025.

Acknowledgments

First and foremost, I want to extend my heartfelt thanks to Oliver Huhn, who first introduced me to this topic back in 2015 and gave me the chance to collect my own samples for this work long before it was even on the table. I deeply appreciate his willingness to always make time for me, no matter how last-minute, and his patience in explaining things until even Grandma Peckbrenner understood. I'm grateful for all the insightful conversations that sharpened my understanding of the subject, the entertaining anecdotes from years of life experience, and his unwavering good humor, regardless of the circumstances, weather, or paperwork.

The work would have been unimaginable without Mara Neudert, who consistently offered encouragement and support. She kept me updated with the latest cat content and was an immense help with the twists and turns of digital data processing, dealing with ones, zeros, and occasionally, decimal years.

I also want to thank Christian Melsheimer for agreeing to be the second reviewer and, most importantly, for the countless conversations about languages, diverse career paths, and all the interesting things that come our way.

I cannot forget Renas Renas, who laid the mental groundwork for this work—Chistole!

Last but not least, my thanks go to Hannah Limburg, who was effectively the decision-maker at the time of enrollment and knew from the start that I would reach the goal.

Abstract

Climate change, driven by anthropogenic greenhouse gas emissions, contributes to the melting of ice sheets, resulting in the rise of the global sea level. This study focuses on Earth's largest ice shelf by volume, called the Filchner-Ronne Ice Shelf (FRIS) in Antarctica. The FRIS plays an important role in buttressing the West Antarctic Ice Sheet (WAIS) and producing Antarctic Bottom Water (AABW), which drives the ocean's thermohaline circulation. Accelerated melting of the FRIS could induce a feedback loop and by that speed up the collapse of the WAIS. The main aim of this work was quantifying basal glacial meltwater (GMW) fractions at the FRIS, and detecting variations between locations and over time. Hydrographic and noble gas data from five different research expeditions to the FRIS in the Weddell Sea between 1995 and 2021 have been analyzed and compared. Conductivity, temperature, and depth recordings were used to identify water masses, and helium and neon were used to compute basal glacial meltwater (GMW) fractions.

Quantification resulted in GMW fractions of up to 1.2±0.1% for the Filchner Trough and up to 0.7±0.1% for the Ronne Depression. Furthermore, it was found that the area over which the GMW fractions could be detected has decreased with increasing distance from the ice shelf front. Yet the GMW remained detectable along the entire Filchner Trough throughout the time series with unchanged magnitude. Determining the Surface Super Saturation (3S), a natural background level of noble gases in seawater is an important part of the GMW calculation. The analysis did show that the 3S value is highly variable (0.96-4.20%) and can fluctuate by several percentage points within a few years. In addition, a source of crustal helium was observed and the annual production of sea ice was estimated.

These results demonstrate that GMW fractions from the FRIS have remained consistent over time, with no evidence of accelerated basal melting. Furthermore, the study introduced a novel method for accurately determining the 3S value, while accounting for the influence of sea ice formation and crustal helium input on noble gas concentrations. These findings underscore the value of noble gases as tracers for GMW and as valuable tools for comparing sea ice production, emphasizing the need for continued research and monitoring of the Weddell Sea to assess the stability of the FRIS.

Table of Content

List of Abbreviations ... 1
1. Introduction ... 2
  1.1 Filchner-Ronne Ice Shelf ... 3
  1.2 Basal Melting ... 5
  1.3 Weddell Sea and Filchner-Ronne Specifics ... 6
    1.3.1 Filchner-Ronne Bathymetry ... 7
    1.3.2 Weddell Sea Hydrography ... 8
    1.3.3 Filchner-Ronne Hydrography ... 9
  1.4 State-of-the-art in Assessing Basal Melting of Ice Shelves ... 10
  1.5 Objectives and Research Question ... 11
2. Methodology ... 12
  2.1 Data Collection ... 12
  2.2 Sampling and Laboratory Analysis ... 13
  2.3 Excess of Helium and Neon ... 14
  2.4 Basal Glacial Meltwater Calculation from Helium and Neon ... 14
  2.5 Additional Helium and Neon Sources ... 16
3. Results ... 18
  3.1 Grouping ... 18
  3.2 Data Assessment ... 18
  3.3 Temperature and Salinity Classification ... 19
  3.4 Helium and Neon Excess Distribution ... 19
  3.5 Basal Glacial Meltwater Fractions ... 23
  3.6 Additional Helium and Neon Sources ... 27
    3.6.1 Crustal Helium ... 27
    3.6.2 Sea Ice Formation ... 29
4. Discussion ... 33
  4.1 Surface Super Saturation 3S ... 33
    4.1.1 Challenges in Determining the 3S Value ... 33
    4.1.2 Natural Variability and Methodological Robustness ... 34
    4.1.3 Implications on GMW Fractions ... 36
  4.2 Basal Glacial Meltwater ... 37
    4.2.1 Filchner Ice Shelf GMW ... 37
    4.2.2 Ronne-Mode and Berkner-Mode ... 39
    4.2.3 Ronne Ice Shelf GMW ... 40
  4.3 Additional Helium and Neon Sources ... 40

4.3.1 Crustal Helium 40
4.3.2 Sea Ice Formation 41
5. Conclusion and Summary 43
6. Outlook 44
7. References 45
8. Appendix 50
A.1 Statistical Tools 50
A.2 Statement about the usage of AI 50

List of Abbreviations

		Page
3S:	Surface SuperSaturation	14
ACC:	Antarctic Circumpolar Current	8
ABBW:	Antarctic Bottom Water	4
AIS:	Antarctic Ice Sheet	2
ASW:	Antarctic Surface Water	8
ASF:	Antarctic Slope Front	8
CDW:	Circumpolar Deep Water	5
EAIS:	East Antarctic Ice Sheet	2
FIS:	Filchner Ice Shelf	7
FRIS:	Filchner-Ronne Ice Shelf	3
GMW:	basal Glacial Meltwater	10
GrIS:	Greenland Ice Sheet	2
HSSW:	High Salinity Shelf Water	5
IPCC:	Intergovernmental Panel on Climate Change	1
ISW:	Ice Shelf Water	5
mWDW:	Modified Warm Deep Water	8
RIS:	Ronne Ice Shelf	7
SAM:	Southern Annual Mode	39
WAIS:	West Antarctic Ice Sheet	2
WDW:	Warm Deep Water	8
WSDW:	Weddell Sea Deep Water	8
WSBW:	Weddell Sea Bottom Water	8
WW:	Winter Water	8

1. Introduction

Climate change is one of the most extensive and urgent issues the world is facing today. Caused by anthropogenic emissions of greenhouse gases into the atmosphere, Earth's climate and temperatures undergo long-term changes. These changes are accelerating, have large-scale impacts, and to a certain extent irreversible consequences. The little time available to react raises the urgency of the topic. According to the Intergovernmental Panel on Climate Change (IPCC), the world must reduce greenhouse gas emissions by at least 45% by 2030 and achieve net-zero emissions by 2050 to limit global warming to 1.5 degrees Celsius above pre-industrial levels (IPCC, 2023). The threshold of 1.5 degrees Celsius was chosen as a compromise between realism and the dire need to minimize the severe effects of climate change.

As a general term, climate science encompasses many disciplines devoted to investigating and understanding global warming. Physical oceanography is a major of these disciplines focusing on the ocean's critical role in regulating Earth's climate system. Acting as a significant heat reservoir, the ocean absorbs and releases energy, with ocean currents being responsible for its global redistribution (called global overturning circulation), influencing regional weather patterns and shaping the climate. The ocean also serves as an important carbon sink of the planet, taking up approximately a quarter of anthropogenic carbon dioxide emissions (IPCC, 2023). Through observational techniques like moorings, satellite altimetry, or CTD measurements and investigative techniques like water sampling, physical oceanographers reveal global temperature and climate trends, enabling scientists to predict the impacts of a warming environment. The aim of this study is quantifying basal melting utilizing data gathered with these techniques.

One of the most prominent consequences of global warming is the melting of the polar ice sheets and the resulting rise of the global sea level. Rising global sea levels endanger ecosystems and human society (IPCC, 2023). Greenland and Antarctica, are home to the only two ice sheets existing today, the Greenland Ice Sheet (GrIS) and the Antarctic Ice Sheet (AIS). Additionally, the AIS can be separated into the East Antarctic and West Antarctic Ice Sheet (EAIS and WAIS respectively). However, the WAIS is a special case of an ice sheet, as its base is in fact on land, but below sea level and is therefore called a marine ice sheet. Notably, Greenland and Antarctica are the biggest freshwater reservoirs of the planet, but they are losing mass (e. g. Janout et al., 2021; Rignot et al., 2019b; The IMBIE team, 2018), with their melting already accounting for up to 20% of the global sea level rise (Heinemann et al., 2017). Bamber et al. (2009) estimate that the AIS alone has the potential to raise the global sea level by 58 meters if it were to melt entirely.

Melting of these ice sheets will not only affect the sea level but also lead to cold freshwater runoff into the oceans and consequently to a slight cooling of the water temperatures. This temperature change by freshwater input is accompanied by a change in salinity and their interplay influences the vertical stratification of ocean water masses. In cold waters, especially at 2°C and below, this stratification is determined by salinity instead of temperature (Nycander et al., 2015). If altered, the stratification can in turn alter the formation of ocean water masses. As the global overturning circulation is based on these large ocean water masses and their global pathways, their disruption can affect the distribution of heat around the globe, potentially leading to changes in weather patterns and the overall climate (Shaw et al., 2023).

Only snow and ice that is on land or locked to land contribute to sea level rise if it melts and finds its way into the oceans, due to isostasy (sea ice, formed on the open ocean for example, does not contribute since it is already displacing its mass as water volume). An interesting ice-ocean interface is the ice shelves, the floating, yet still connected extension of an ice sheet. However, as they are floating ice shelves also do not directly contribute to sea level rise. Nevertheless, ice shelves play an important role in controlling the flow speed of glaciers and ice streams. They can become unstable and break apart, for example, because of substantial mass loss. The result could be a reduced buttressing effect on ice on land leading to faster ice flow into the ocean and thus to a rising sea level (Bamber et al., 2009; Shepherd et al., 2012). The area of ice shelves of the GrIS is neglectable compared to those of the AIS. The latter covers approximately 75% of Antarctica's coastline, spanning an area of roughly 1.561 million square kilometers, which is comparable in size to the complete GrIS (Rignot et al., 2013). The majority of the Antarctic ice shelf area, roughly two-thirds, is part of the marine WAIS (Andreasen et al., 2023). These floating ice bodies gain mass by the inflow of ice from glaciers, accumulation of snow, and the formation of marine ice by freezing of sea water on their undersides. Conversely, they undergo mass loss through calving icebergs at their outer edges, basal melting, sublimation, and wind-driven drift on their surfaces (Rignot et al., 2013). Therefore, ice shelves, especially the large Antarctic ones, are an important matter of science, especially regarding the controversially discussed tipping points (IPCC, 2023).

1.1 Filchner-Ronne Ice Shelf

At the southern end of the Wedell Sea, on the Antarctic continental shelf is the world´s largest ice shelf by volume, the Filchner-Ronne Ice Shelf (FRIS) (Fox et al., 1994). Figure 1 gives a geographical overview, indicating bounding regions and also important geological features (Ronne Depression, Filchner Depression). Gardner et al. (2018) calculated that the FRIS accounts for roughly 11% of the total ice discharge from the AIS. The thickness of the ice shelf is more than 1,700 m at the grounding line and reduces to 200-400 meters at the Ronne calving front and 400-600 meters at the Filchner calving front (Bedmap2, Fretwell et al., 2013). Fox et al. (1994) report the area of the FRIS to be 449,220 km², a third of the total shelf area in Antarctica, not considering ice rises and ice rumples. Ice rises and rumples are areas where an ice shelf comes in contact with a seabed feature. In case of rises, the ice then flows around it, while for ice rumples it also flows across (Matsuoka et al., 2015). An important area where the ice shelf flow is altered is Berkner Island. Technically, because the ice flows around but not over Berkner Island, it is an ice rise and therefore also referred to as Berkner Ice Rise.

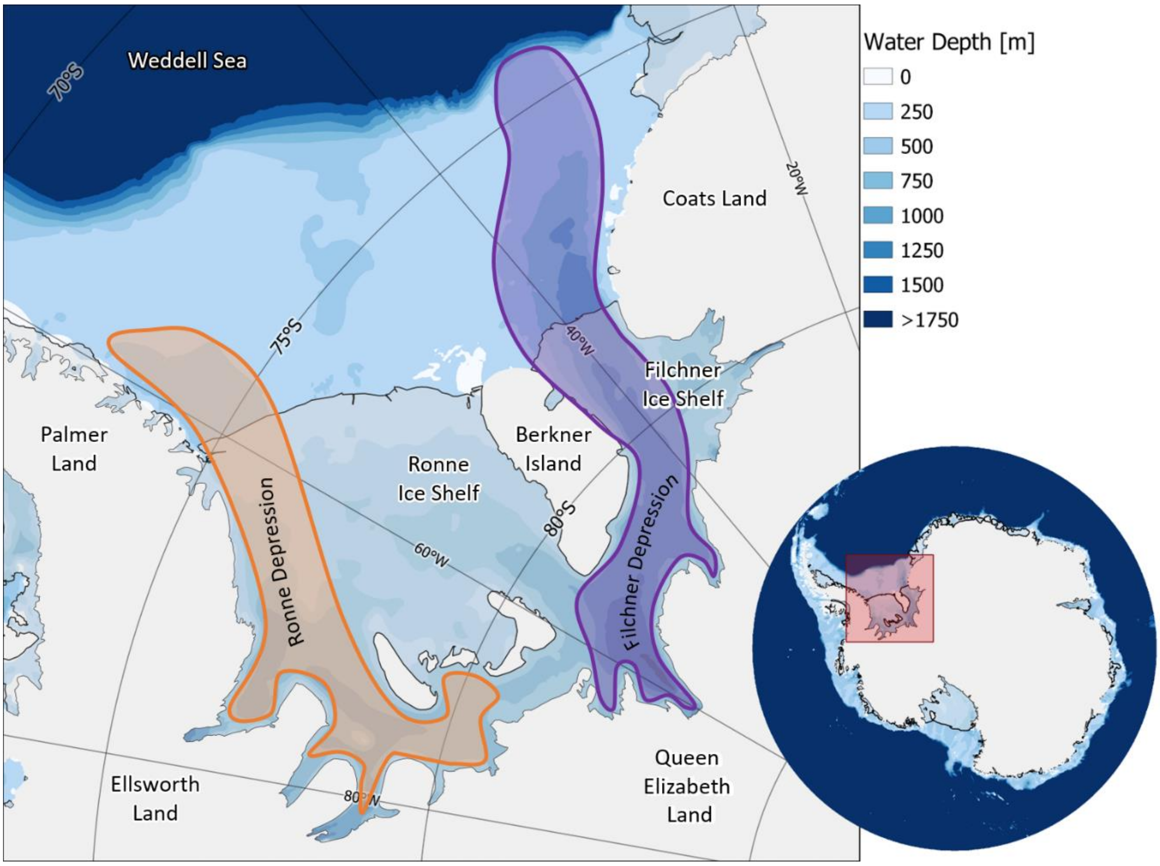

Figure 1: Overview of the research area in the Southern Ocean. Enlarged is a cut-out of the FRIS in the Weddell Sea with its surrounding lands. Important locations are the Filchner Depression shaded and outlined in purple, which extends from the continental shelf break to the southern end of the embayment, and the Ronne Depression at the western coastline shaded and outlined in orange. The solid black line represents the ice shelf fronts. The ice shelf area is slightly grey-shaded. Almost the entire Filchner Ice Shelf is underlain by the Filchner Depression. Map was created with Quantarctica (Matsuoka et al., 2021)

Reese et al. (2018) pronounced the crucial role of the FRIS in buttressing the WAIS. With models they showed a significant accelerated flow of grounded ice, contributing to sea level rise should the FRIS destabilize. Consequently, a collapsing FRIS would further affect water stratification and Antarctic Bottom Water (AABW) formation. As AABW is one of the key drivers of the world's ocean currents and thermohaline circulation (Meredith, 2013), it is desirable to investigate the FRIS and the processes destabilizing it. According to Rignot et al. (2013) and Paolo et al. (2015) basal melting (melting of the ice shelf from below) has accelerated during the last decades. The former claims basal melting accounts for 55±10% of the total mass loss of all Antarctic ice shelves, contrasting the traditional estimate of 10 to 28%, representing an increase of 0.6 to 6.5 times.

1.2 Basal Melting

Stanley S. Jacobs introduced the term basal melting in the 1970s and 1980s which has since been adopted in the scientific community. However, the term is not used uniformly in science and can cover any process that induces melting on the underside of an ice sheet. As ice shelves float in the ocean, basal melting in context with ice shelves describes melting due to contact with ocean water above the melting point. Usually, the surface water temperature in the Southern Ocean close to the ice shelves is around -1.8° to 0°C and therefore not high enough to melt ice on a large scale. It is the so-called ice-pump mechanism (Figure 2) that induces basal melting at the deeper sections of the shelves.

When sea ice is formed at the surface the salinity of the seawater increases, causing the water to sink and forming a water mass known as High Salinity Shelf Water (HSSW). Depending on the formation region, portions of the HSSW mix with other water masses and ultimately form AABW. Other portions of the HSSW follow the topography under the ice shelf, eventually reaching its base. Under high pressure, the water is still above the melting point of the ice and therefore begins to melt the underside of the ice shelf. Due to the addition of fresh water, the salinity in the seawater decreases and the water rises along the ice shelf's underside transforming into Ice Shelf Water (ISW) (Figure 2). Subsequently, ISW may evolve into AABW through further processes as described by Foldvik (1985). A total of 60% of AABW is formed by these mechanisms (Orsi et al., 2002, 1999).

Coring work and chemical analysis by Oerter et al. (1992) revealed the large extent of basal melting occurring at the FRIS. Hellmer et al. (2012) and Timmermann & Hellmer (2013) pointed out that changes in ocean currents and water properties could intensify the inflow of warm water below the FRIS and consequently enhance basal melting by a factor of up to 4 to 6. This is in line with the overall prognosticated rates by Rignot et al. (2013) mentioned earlier. However, at present a strong front of dense and cold waters on the Antarctic continental shelf of the Weddell Sea prevents the inflow of warm Circumpolar Deep Water (CDW) protecting the ice shelf from an even stronger acceleration of basal melting (Daae et al., 2020). Nevertheless, as basal melting plays a key role in destabilizing the largest ice shelf it is important to estimate its amount for future prognosis.

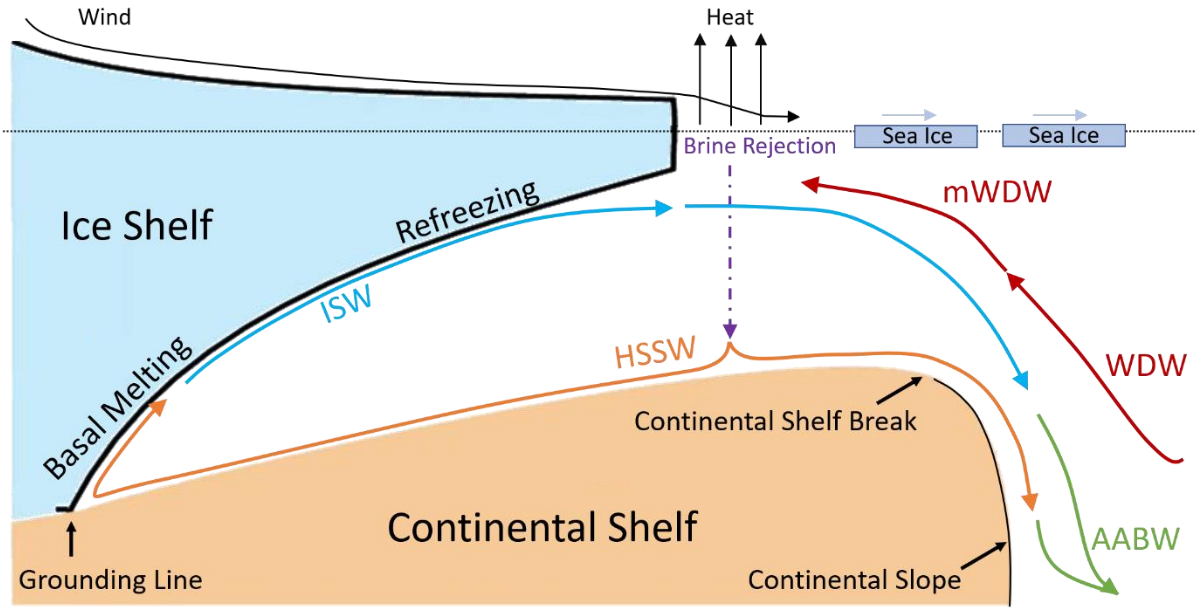

Figure 2: Ice pump mechanism and exemplary overview of the hydrography on the Filchner-Ronne continental shelf. Sea ice forms and is pushed away by strong offshore winds. Because of brine rejection (purple), HSSW (orange) is formed. Some HSSW flows across the continental shelf break and ultimately becomes ABBW (green). Other portions of HSSW follow the topography of the continental shelf into the ice shelf cavity. Because the HSSW is above the freezing point it induces basal melting and forms ISW (blue). Parts of the ISW might refreeze, but it mostly follows the underside of the ice shelf until it also flows down the continental slope and eventually becomes ABBW. WDW enters the shelf, cools because of ambient water masses, and becomes mWDW. Note, that this scenario is altered to fit the situation at the FRIS. At other ice shelves, WDW might enter farther onto the continental shelf and into the ice shelf cavity. To highlight the ice pump-related processes, as well as the characteristic ASF, intermediate water masses are disregarded and not shown) After Center for Coastal Physical Oceanography (2016).

1.3 Weddell Sea and Filchner-Ronne Specifics

Despite the significance of the processes underneath the ice shelves for AABW formation and global ocean circulations, accessing the cavity below an ice shelf to evaluate the presence of the water masses and the relative importance of the processes described above is a difficult and tedious task. Hence, most water samples are taken in the open ocean, where research vessels can operate with minor difficulties, despite sea ice cover. Nevertheless, it is necessary to know the bedrock elevation and shelf ice thickness to assess oceanographic processes in the ice shelf cavity accurately. Both, the bathymetry, and based on that the hydrography, are crucial to connect water mass properties observed in front of an ice shelf to the amount of basal melting. Ridges and troughs can block or channel the movement of dense water, impacting melting patterns. Additionally, the shape of the cavity beneath the ice shelf influences the formation and outflow of dense ISW. Therefore, accurately mapping this sub-ice bathymetry is essential for modeling ice shelf-ocean interactions.

1.3.1 Filchner-Ronne Bathymetry

The FRIS covers roughly half of the continental shelf of the Filchner-Ronne embayment (Bedmap2, Fretwell et al., 2013) with Figure 3 giving an overview of the bathymetry. The most prominent bathymetric features are the Ronne Depression and the Filchner Depression (orange and purple shading respectively in Figure 1; dotted black lines in Figure 3 to not obscure the bathymetry). The former begins in front of the western end of the Ronne Ice Shelf (RIS), following the coastline of Palmer Land and Ellsworth Land in an arc shape. The other extends from the continental shelf break to Queen Elizabeth Land, connecting the open ocean with the deepest part of the Filchner Ice Shelf (FIS) cavity. It is noteworthy that almost the entire FIS is underlain by the Filchner Depression, whereas the Ronne Depression underlies only roughly a third of the RIS. From north to south, the sea floor elevation drops within these depressions with the deepest point, around 2000 meters, located at the southern end of the Filchner Depression (Rosier et al., 2018). Due to the inability of airborne radar to penetrate the ice, bathymetric data for the sub-ice bedrock is limited. Ongoing research, such as by Rosier et al. (2018), aims to improve bathymetric accuracy.

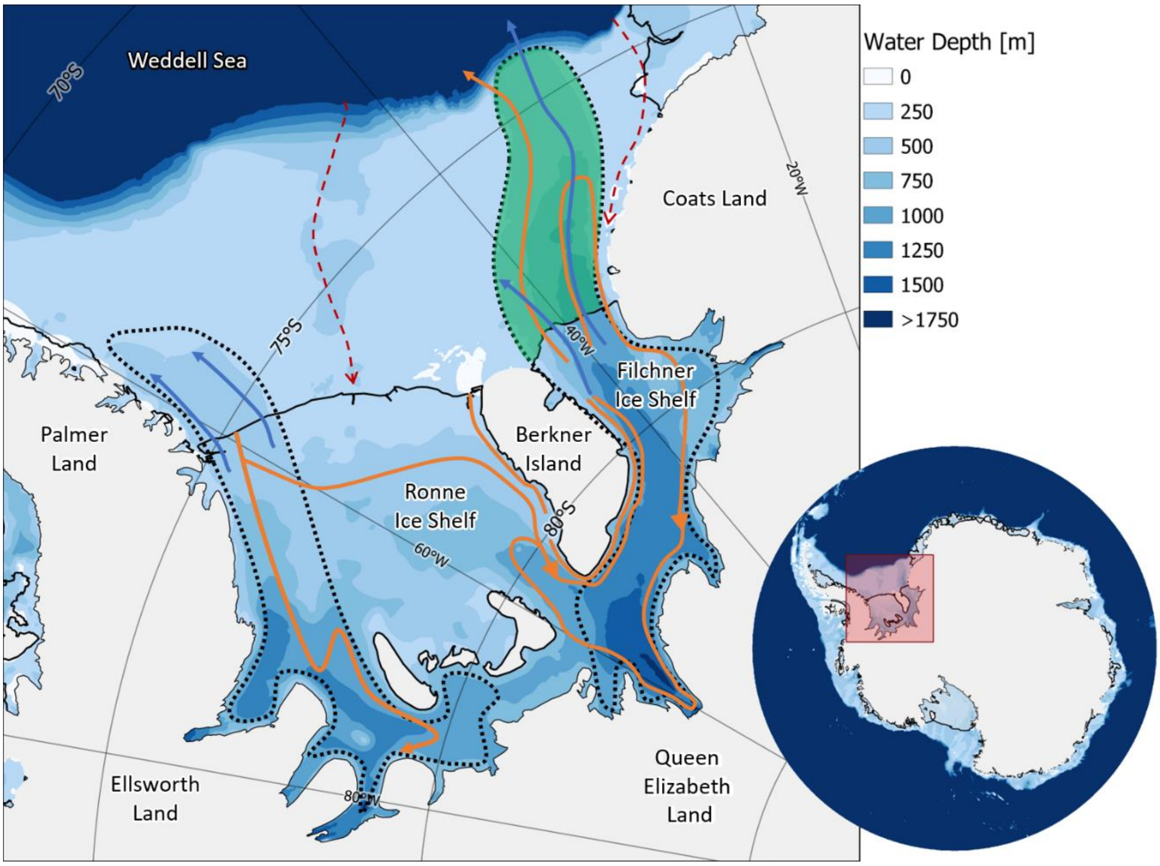

Figure 3: Schematic of the flow regimes on the continental shelf. The red dashed arrows show the major mWDW inflow, centrally in front of the RIS and at the coastline of the Coats Land. The thin black line shows the ice shelf front. Orange and blue arrows indicate the HSSW and ISW flow respectively. The dotted black lines outline the Ronne Depression and Filchner Depression. The green-shaded area is the Filchner Trough. Figure after Nicholls et al. (2009). Map was created with Quantarctica (Matsuoka et al., 2021)

Similar to basal melting, there is no consistency in oceanographic literature about the terms Filchner Depression and Filchner Trough which are often used interchangeably, disregarding any geological context. For the remainder of this thesis, Filchner Depression will describe the entire feature from the continental shelf break towards the deepest elevations below the FIS as described in the paragraph above. Filchner Trough on the other hand will only refer to the part of the Filchner Depression between the front of the FIS and the continental shelf break (green shaded area in Figure 3). Although the two depressions are important for circulation and are extensively illustrated here, the extent shown is only an assumption based on the bathymetric data from Bedmap2 (Fretwell et al., 2013).

1.3.2 Weddell Sea Hydrography

The overall circulation pattern around Antarctica is cyclonic (clockwise), known as the Antarctic Circumpolar Current (ACC). The ACC is primarily composed of cool and fresh Antarctic Surface Water (ASW) above a relatively warm (0-2°C) and salty core of Circumpolar Deep Water (CDW). Below the CDW is the AABW, the densest water mass in the global ocean circulation. In the eastern regions of the Weddell Basin, the CDW enters a large-scale ocean circulation called the Weddell Gyre (Ryan et al., 2016). The gyre also rotates cyclonically and governs the general directions of water flow in the Weddell Sea. Within the gyre the CDW becomes cooler (0-0.8°C) and less saline, forming Warm Deep Water (WDW). WDW is also considered the Weddell Sea derivate of the CDW and occupies the intermediate layer (200-1200m) (Daae et al., 2020). The Antarctic Slope Front (ASF), an oceanographic feature of the Antarctic shelf break, acts as a natural barrier, protecting the shelf regions from the WDW. At the ASF cool, dense waters flow from the embayment over the shelf break, and due to their density prevent the inflow of other water masses. During the Antarctic winter, the surface temperature cools the ASW down to the freezing point, forming a water mass called Winter Water (WW). Partial mixing of the WW with the underlying WDW, results in an intermediate water mass, referred to as modified Warm Deep Water (mWDW) (Foster and Carmack, 1976). Despite the ASF, mWDW was observed on the Filchner-Ronne embayment, entering at two locations: one shallow continental shelf along the coast of the Coats Land and centrally via the Ronne continental shelf break (dashed red arrows in Figure 3, respectively). While the central inflow of mWDW in front of the RIS is well documented (Foldvik et al., 2001; Gammelsrød et al., 1994), the inflow in front of the Filchner Ice Shelf (FIS) is highly variable (Ryan, 2016; Ryan, 2020; Darelius, 2016). Overall, the influence of mWDW on the FRIS is debated (Janout et al. 2021). The cool and dense water masses flowing down the continental shelf mix with WDW and form Weddell Sea Deep Water (WSDW). By further mixing with the very dense HSSW, WSDW becomes Weddell Sea Bottom Water (WSBW). WSBW, the coldest and densest water of the Weddell Sea, ultimately becomes

AABW as it leaves the Weddell Gyre. Therefore, the dense water masses of the continental shelf (HSSW and ISW) and their formation (ice-pump, Figure 2) are essential for the AABW formation.

1.3.3 Filchner-Ronne Hydrography

The Weddell Sea is characterized by robust catabatic winds and extensive permanent sea ice cover. During austral winter strong winds push newly formed sea ice away from the FRIS exposing the seawater to the atmosphere and enabling new sea ice formation (Paul et al., 2015). This setup makes it the "sea ice factory" of the Southern Ocean, but it also renders the FRIS susceptible to basal melting.

Because of brine rejection during sea ice formation, HSSW forms from WW. From here, the HSSW is assumed to evolve in two general ways, ultimately forming AABW. Gill (1973) was the first to propose that some HSSW does not enter the ice shelf cavity. Foster and Carmack (1976) developed this idea further and concluded that the HSSW mixes with other water masses and directly evolves into AABW. Other parts of the HSSW follow the topography under the ice shelf, eventually reaching its base (ice-pump Figure 2). Subsequently, the ISW that forms as a result of basal melting evolves to ABBW too, after crossing the continental shelf break and entering the Weddell Gyre (Foldvik, 1985).

The HSSW establishes distinct circulation patterns on the continental shelf (Figure 3) (Nicholls & Østerhus, 2004; Nicholls et al., 2009). Below the RIS, the HSSW flows southward along the eastern flank of Berkner Island and within the Ronne Depression. Below the FIS, it follows the eastern flank of the Filchner Depression into the cavity of the FIS, then moves northward, and eventually merges with HSSW from below the Ronne Ice Shelf at the southwestern tip of Berkner Island. During this circulation, the HSSW is partially converted to ISW. The ISW exits the ice shelf cavity via the Filchner Trough towards the continental slope, and around the eastern flank of Berkner Island flowing above the HSWW because of its lower density compared to the HSSW (blue arrows within the Filchner Trough in Figure 3). In the north, the ISW flows down the continental slope eventually evolving to AABW (Foldvik, 1985). Therefore, the formation of ISW from HSSW and its subsequent export as AABW are critical processes in global ocean circulation and climate. Additionally, there are two outflows of ISW at the Ronne Depression. One is at the eastern flank (Nicholls, 2004), and one is newly detected at the western flank of the depression (Janout et al.,2021) (blue arrows within the Ronne Depression in Figure 3). However, Janout et al. (2021) pointed out, that the ISW flowing out of the Ronne Depression is quickly mixing with ambient water masses and is unlikely to make its way to the continental shelf break and thus contrasts the conditions at the FIS. The ISW is the water mass in which the basal meltwater can be detected.

1.4 State-of-the-art in Assessing Basal Melting of Ice Shelves

Regardless of the global importance of the Weddell Sea and the FRIS in particular, the measurement coverage of hydrographic and bathymetric data is sparse, because of its inaccessibility. This, together with the complex structure below the shelves, makes it generally difficult to assess the types of melting of ice shelves. Multiple authors report methods to estimate the mass loss of ice shelves: remote sensing techniques, sometimes supported by models (Hellmer, 2004; Paolo et al., 2015; Rignot et al., 2013; Schodlok et al., 2016; Timmermann & Hellmer, 2013); heat and salt observations together with numerical models (Jacobs et al., 2011; Nicholls et al., 2001, 2006; Nicholls & Makinson, 1998; Nicholls & Østerhus, 2004; Nicholls et al., 2009); phase-sensitive radar systems, pRES (Corr et al., 2002).

A promising approach for investigating basal melting of ice shelves involves analyzing the concentrations of helium and neon in the seawater (e. g. Hohmann, 2002; Huhn 2008; Schlosser, 1986). Helium and neon have a stable concentration and ratio to each other in the atmosphere. When it snows, both gases are trapped within the snow cover on land, resulting in gas concentrations within the snow corresponding to those of the atmosphere (e.g., Hohmann, 2002; Huhn 2008; Schlosser, 1986). Over time, the snow compacts to firn and further to ice, effectively trapping the helium and neon within the ice sheet. The influence of gravity, mass, and topography guides the ice flow toward the ocean, where it eventually becomes part of the ice shelf. As the ice melts, helium and neon are released and dissolve in the seawater. However, unlike at the ocean's surface where the gases would equilibrate with the atmosphere instantaneously, below the ice shelf, the hydrostatic pressure causes helium and neon to dissolve completely in the water.

As a result of this process, there is an excess of helium and neon in the water compared to surface water. Loose & Jenkins (2014) call this excess a saturation anomaly. The saturation anomaly describes the observed gas content regarding the expected gas content if the solubility is in equilibrium. The authors state the anomaly is as high as 1280% for helium and 890% for neon. By analyzing the excess of helium and neon relative to their equilibrium state, researchers can quantify the fraction of basal Glacial Meltwater (GMW), offering valuable insights into the extent of basal melting occurring beneath the ice shelves and its further pathways. While basal melting, as described earlier, refers to melt generated by contact with seawater above the freezing point, GMW also includes melt generated on the continent by processes beneath the ice sheet. The ability to trace the pathways of the GMW is a major advantage of this method compared to satellite data or modelling. Over the last decades, the mass loss of FRIS has increased significantly (Paolo et al., 2015; The IMBIE team, 2018). Huhn et al. (2018) used water samples from directly below the FIS for the first time and reported a maximum of 3.6% GMW at the ice shelf base and inferred a mass loss because of basal melting of 177 ± 95 Gt/y. However, the mean GMW fractions underneath the FIS calculated by Huhn et al. (2018) was 1.3%. This is consistent with findings by Janout et al. (2021) who did not have access to samples from below the FIS and reported GMW fractions up to 1% directly in front of the FIS.

1.5 Objectives and Research Question

Processes in the Weddell Sea, particularly beneath the FRIS, the largest ice shelf on Earth, are major producers of AABW. As one of the driving forces of global ocean circulation AABW, in turn, has a significant impact on the climate. If the FRIS becomes unstable, as some authors have suggested, it could have severe consequences. Therefore, monitoring the FRIS in the Weddell Sea is essential to assess its impact on the entire climate system.

The primary objective of this research is to quantify the basal Glacial Meltwater (GMW) originating from the Filchner-Ronne Ice Shelf (FRIS) and to explore its distribution using noble gas tracers, specifically helium and neon. This study seeks to address key research questions: What are the major challenges of applying this method to a broad variety of samples? Are there significant variations in GMW fractions from the FRIS over time and geographically? A novel approach is employed to assess background gas saturation levels, which is critical for accurate GMW quantification. The research also assesses how factors like sea ice formation and crustal helium influence GMW values. Additionally, the potential of noble gases as tracers for the amount of sea ice formation will be investigated. Ultimately, the study aims to contribute to a better understanding of the stability of the ice shelf and its potential impact on global sea levels and ocean circulation.

2. Methodology

2.1 Data Collection

The data utilized in this study were obtained from water samples collected during five separate research cruises conducted aboard the German research vessel (RV) Polarstern. The cruises took place in austral summer from 1995 to 2021. Hydrography and tracer data are published on, or in the case of the latest cruise submitted to the PANGAEA data repository. One set of tracer data is an exception and has been obtained from personal communication with Dr. O. Huhn, IUP Bremen. For better readability, cruise names, dates, and citations are given in Table 1. Subsequently, in this work, the data will be referred to by the respective year the cruise ended in, e. g., 1995, 2014, 2016, 2018, and 2021. Figure 4 depicts the sampling locations relative to the corresponding cruises. Furthermore, Figure 4 shows how the data was grouped and the position of plotting transects, both will be discussed in the results section.

Cruise Name	Date	Hydrography	Tracer Data
ANT XII/3	05.03.1995 - 19.03.1995	Schröder et al., 2010 10.1594/PANGAEA.742581	Roether et al., 2017 10.1594/PANGAEA.883832
ANT XXIX/9	20.12.2013 - 23.02.2014	Schröder et al., 2014 10.1594/PANGAEA.833299	Huhn et al., 2017 10.1594/PANGAEA.883799
PS 96	06.12.2015 - 14.02.2016	Schröder et al., 2016 10.1594/PANGAEA.859040	Personal Communication
PS 111	19.01.2018 - 14.03.2018	Janout et al., 2019 10.1594/PANGAEA.897280	Huhn et al., 2021a 10.1594/PANGAEA.930718
PS 124	03.02.2021 - 30.03.2021	Tippenhauer et al., 2023 10.1594/PANGAEA.961780	Submitted

Table 1: Cruise names, dates, and citations of the published hydrography and tracer data.

All expeditions primarily focused on the West Antarctic region, specifically the Weddell Sea surrounding the Filchner-Ronne Ice Shelf. During each cruise water samples were collected from tightly spaced locations and depths to facilitate subsequent analysis. The aim was to get as close to the ice shelf front as possible and take samples in transects along the front and in a parallel fashion at increasing distances from the front. It was, however, not always possible to reach the ice shelf front, as the dense sea ice cover in this region limited the southward advancement of the vessel.

2.2 Sampling and Laboratory Analysis

The water samples were taken with sampling bottles mounted to a CTD-Rosette. Salinity and temperature were determined on-site by personnel of the Alfred Wegener Institute, Bremerhaven, Germany. In the lab of the Institute of Environmental Physics Bremen (IUP), Germany, the samples were analyzed for parameters such as helium and neon concentrations and others. The water measurements are calibrated to an air standard manufactured by IUP personnel operating the lab (Sültenfuß et al., 2009). The measurement accuracy of the noble-gas mass-spectrometer at the IUP is <0.5%. When measuring helium and neon concentrations, multiple isotopes are recorded. These are ^{3}He and ^{4}He for helium, ^{20}Ne and ^{22}Ne for neon. However, for this analysis, only the total concentrations are utilized. Specific isotopes are therefore not denoted, and "He" and "Ne" are used to represent the entire helium and neon concentrations, respectively.

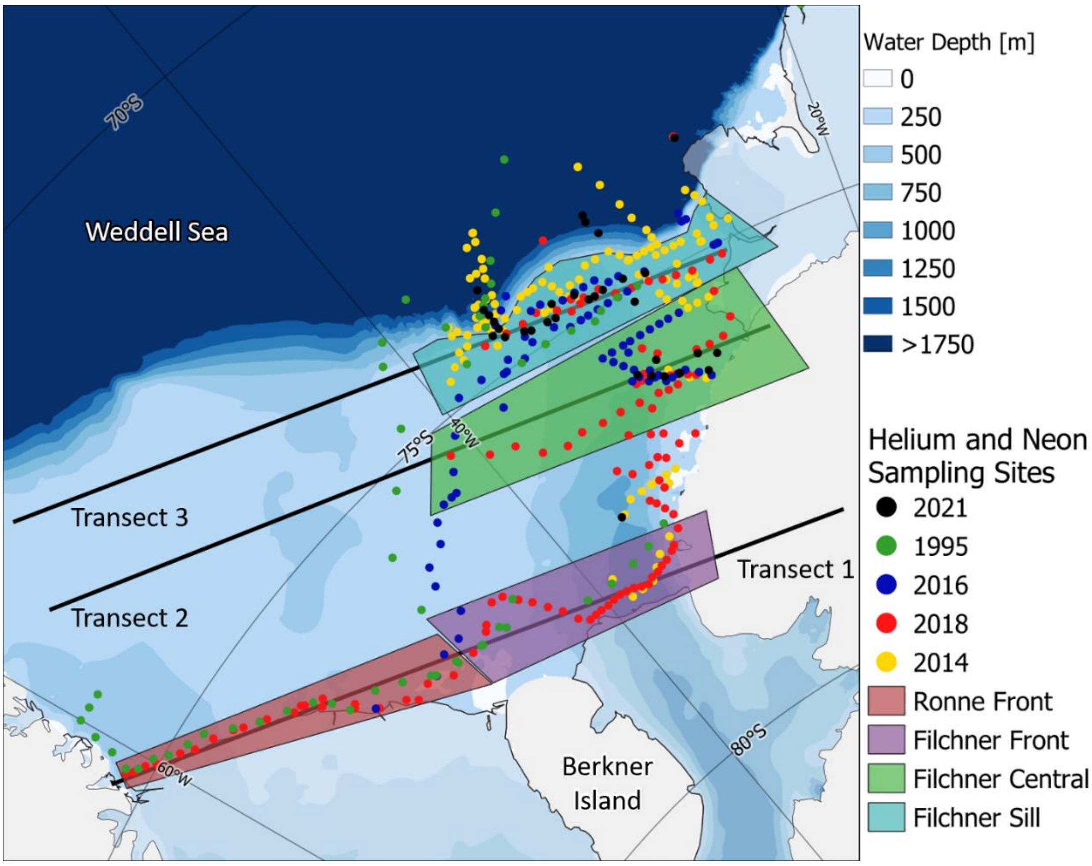

Figure 4: Overview of all sampling sites in the research area of the five cruises. Given are also the regions the data is grouped in and the transects used for depth-over-distance plots as described in the results section. In this figure, all sampling locations are shown, including those where no helium or neon was sampled. Map was created with Quantarctica (Matsuoka et al., 2021)

2.3 Excess of Helium and Neon

The solubility of helium and neon in water is extremely low compared to other gases, e.g., O_2, or Ar. According to Weiss (1971), the solubility of the gases ranges from 1.5-2.2nmol/kg for helium and 5.8-10.0nmol/kg for neon, both under atmospheric conditions and in equilibrium. This is the maximum theoretical amount of helium and neon that can dissolve in water when the water and atmosphere are in equilibrium, considering specific temperature and salinity conditions, and is called the equilibrium value. Both, the salinity and the temperature of the water affect the solubility of the gases in an inversely proportional way, explaining the given ranges.

However, there are mechanisms for adding helium and neon to the seawater, therefore their concentrations can be off the equilibrium value. This excess of helium and neon will be expressed in percent as ΔHe and ΔNe respectively. Equation 1 depicts the calculation of ΔHe and ΔNe with ΔGas being the respective element. The observed helium and neon concentrations are denoted as Gas_{obs} (accuracy <0.5%), whereas Gas_{eq} is the equilibrium value as a function of temperature and salinity according to Weiss (1971). This means, that if there were no mechanism for adding helium and neon to the seawater, ΔGas would be zero according to Equation 1.

$$\Delta Gas\ \% = \left(\left(\frac{Gas_{obs}}{Gas_{eq}}\right) - 1\right) * 100 \quad with \quad Gas_{eq} = f(T,S) \qquad \text{Equation 1}$$

Note, that loss of helium and neon can only happen by equilibration of oversaturated water with the atmosphere.

2.4 Basal Glacial Meltwater Calculation from Helium and Neon

To assess the amount of GMW, the helium and neon data have to be adjusted for enrichments that can be reliably quantified and do not originate from melted ice. Rhein et al. (2018) implemented a method to calculate GMW fractions from helium and neon concentrations.

In the first step, all samples are adjusted for a natural oversaturation of helium and neon (Loose & Jenkins, 2014). This oversaturation is the result of a process called bubble injection. Breaking waves inject air containing helium and neon into the water, leading to a local background of excess gases. For the remainder of the study, this background excess will be called Surface SuperSaturation (3S) and has to be subtracted. The 3S is determined by averaging the helium and neon values of samples taken at the surface of the water column. Ideally, to avoid interference with already GMW-enriched water, sampling locations several hundred kilometers away from the shelf ice front should be chosen to obtain the 3S. However, there are not always suitable locations, or amount of data to determine the 3S reliably.

Huhn et al. (2021b) and Rhein et al. (2018) reported 3S values of 5.0% for helium and 4.1% for neon observed in the Fram Strait in the Arctic Ocean. In a preparatory project for this master thesis, however, it became evident that using the 3S literature values yields meaningless results. The reasons are the temporal (multiple years) and the spatial (Arctic vs. Antarctic) variations of the ocean properties.

Nevertheless, because of the lack of available data and the necessity of a 3S value, I assume that vertical mixing does not suffice to transport GMW-enriched water from great depths very close to the surface. This is supported by the highly negative δ^3He ratio of the used surface samples. At the sea floor, hydrothermal vents can release ^3He into the water, enriching the water above the equilibrium value. This is usually the case for CDW in the Southern Ocean. As WDW (the Weddell Sea deviation of CDW) enters the continental shelf, positive δ^3He should be observed at the sea surface if sufficient upwelling occurs. However, the δ^3He ratio of the used samples is negative and close to the ratio expected in Antarctic surface water (-1.8), leading to the conclusion that neither WDW nor GMW were upwelled to the surface. Therefore, even values obtained close to the ice shelf front should be unaffected by helium enrichment from basal melting.

Neon on the contrary can be affected by sea ice formation (see paragraph on additional sources) and values taken at the surface may bear a signal of this process, especially close to the ice shelf front as this is the primary sea ice formation zone (Paul et al., 2015). Yet, this problem can be tackled by considering Loose & Jenkins (2014) who simulated the process of bubble injection to represent its effect on the saturation of noble gases in seawater beyond the atmospheric equilibrium. Their simulation showed that ΔHe is 1.32 times greater than ΔNe, with saturation excesses of 11.6% and 8.8%, respectively. The important information from their approach is the ratio of the excesses, which can be used to derive a 3S value for neon based on the 3S value of helium.

Table 2 shows an overview of the δ^3He values, the 3S values for helium, and neon, and their standard deviations for each year retrieved from the respective data set. Table 2 also indicates the neon value derived from helium based on the description above. The derived 3S values for neon are lower than the measured values for each dataset. These differences suggest that the non-derived 3S values come from samples enriched with neon because of sea ice formation. Therefore, deriving a 3S value for neon is a reasonable approach, as it prevents excessively high 3S values and, consequently, an underestimation of GMW fractions. Hence, for the final GMW calculation, the derived 3S values were used.

Year	3S He [%]	SD He	3S Ne [%]	SD Ne	Ne derived [%]	δ^3He [%]	SD δ^3He
1995	0.96	1.20	0.83	0.85	0.73	-1.32	0.33
2014	3.88	1.38	3.55	1.11	2.94	-1.76	0.91
2016	4.05	0.94	4.03	1.72	3.07	-1.49	1.52
2018	4.20	1.33	4.42	1.48	3.18	-1.60	1.75
2021	1.24	0.70	1.42	1.18	0.94	-1.50	1.01

*Table 2: Overview of the 3S values for helium and neon, the **δ^3He ratios,** their standard deviations (SD), and the derived neon 3S value.*

The next step is subtracting the individual equilibrium value, calculated by the solubility function after Weiss (1971), from all samples. Any further excess of He and Ne concentrations beyond the 3S value and the equilibrium solution serve as indicators of GMW, where helium and neon were dissolved into the melt water because of hydrostatic pressure. Pure meltwater would contain 1280% more He and 890% more Ne than expected in an equilibrium state (Loose & Jenkins, 2014). Consequently, fractions of GMW would result in proportional fractions of excess helium and neon. However, this does not consider additional sources of helium and neon that cannot easily be quantified and addressed (see next paragraph). Equation 2 presents how GMW (%) was computed. Pure GMW is added and denoted as PMW in the equation to infer the correct fractions. According to Loose & Jenkins (2014), PMW has a helium and neon concentration of 25.7 nmol/kg and 90.1 nmol/kg, respectively.

$$GMW\ \% = \left(\left(\frac{(Gas_{obs} - Gas_{eq} * (1 + \left(\frac{3S}{100}\right)))}{(PMW - Gas_{eq} * 1 + \left(\frac{3S}{100}\right)))}\right) * 100\right) \quad with\ Gas_{eq} = f(T, S) \qquad \text{Equation 2}$$

When calculating GMW an uncertainty of <0.05% is induced by the measurement accuracy of <0.5%, yet, the largest uncertainty in this calculation is caused by the standard deviation of the 3S value (Table 2). To account for the annual variability of the 3S value the standard deviation was conservatively estimated by averaging over all years (SD = 1.1), resulting in an error margin of the GMW calculation of ±0.08%. The uncertainties from the concentration measurement and 3S standard deviation are combined in quadrature and yield a total uncertainty of ±0.1% (rounded up from 0.094% to be on the safe side).

2.5 Additional Helium and Neon Sources

The influence of an additional helium or neon source can be made visible by calculating Δ(He/Ne). Equation 3 shows how Δ(He/Ne) was calculated from He_{obs} and Ne_{obs} and the equilibrium values He_{eq}

and Ne_{eq}. The determining part is the ratio of the observed ratio and the equilibrium ratio of the gases. The same measurement uncertainties described in the previous paragraph apply, resulting in an error margin of ±0.7% for Δ(He/Ne).

$$\Delta\left(\frac{He}{Ne}\right)\% = \left(\left(He_{obs}/Ne_{obs}\right)/\left(He_{eq}/Ne_{eq}\right) - 1\right) * 100 \qquad \text{Equation 3}$$

Significant positive values (above 2%) of Δ(He/Ne) reflect a source that only contributes additional helium and negative values indicate the presence of sources that only contribute additional neon (Huhn et al., 2021b). Values between 0% and 2% cannot confidently be attributed.

A common source for additional helium is α-decay of uranium and thorium. This creates ^4He in the crust below the ice sheet and can accumulate in the lower part of the ice sheet, up to 300m (Craig & Scarsi, 1997). When this lower part of the ice sheet melts, either on land by geothermal heat and friction or by basal melting in contact with seawater, the additional helium dissolves in the seawater, too.

When significantly more neon is added Δ(He/Ne) becomes negative (Equation 3). The only other possible source of neon is sea ice formation (besides basal melting, which affects helium in the same fashion as neon and would therefore not alter Δ(He/Ne)). Helium gets incorporated into the ice lattice during sea ice formation while neon is partly rejected, similar to sea salt. The result is a higher concentration of neon compared to that of helium (Hahm et al., 2004). Because of this circumstance, the neon 3S value should be derived from helium and not be based on surface measurements of neon.

3. Results

3.1 Grouping

As shown in Figure 4 in the methods section, the sampling sites were grouped into four regions, labelled as follows: (1) Ronne Front, (2) Filchner Front, (3) Filchner Central, and (4) Filchner Sill, accounting for the spatial variations of the sampling sites and to ensure a more comprehensive representation. The regions were chosen so they encompass the majority of samples, which are mostly taken in transects relatively parallel to the ice shelf front (roughly in east-west direction). This is because the ice shelf front is the closest a research vessel can get to the ice shelf base, where basal melting occurs. Additionally, as described in the introduction, sea ice formation, which affects neon concentrations, predominantly takes place in front of the ice shelf. The general direction of in and outflow of water in front of the ice shelf is south and northward respectively (Figure 3), resulting in a dilution of the signature of basal melting with increasing distance from the ice shelf front. Dilution happens because of mixing with other water masses and entrainment of ambient water, indicated by trace element concentrations. Therefore, parallel transects to detect and display spatial variations are most meaningful. Nevertheless, the transect directly at the ice shelf front was split into two regions, because they resemble two very different regimes (Ronne Front and Filchner Front). It has to be noted that only the 1995 and the 2018 cruises made it to both ice shelf fronts, and the 2014 cruise to parts of the FIS front. Helium and neon concentrations, however, were not sampled at the FIS front in 1995. On all cruises, plenty of samples were collected close to the continental shelf break. Region (4) was specifically chosen to exclude all samples taken on the continental shelf slope or the Weddell Basin. This exclusion was necessary because tracing GMW in these areas would primarily assess currents and flow directions within the Weddell Gyre, which falls outside the scope of this work.

For the final GMW illustration samples between regions (2) and (3) are neglected because they are either taken in a north-south direction (2016), are not sufficient for an east-west section (2021), or are redundant as already longer, more representative east-west profiles exist in their vicinity (2014 and 2018). This is the reason, for example, why the temperature vs. salinity analysis will show Filchner Front samples from 1995, but those do not appear in the GMW analysis.

3.2 Data Assessment

The data was assessed beforehand, to exclude biased or irrelevant samples. The excluded data encompass samples not in the declared regions, where helium and neon were not sampled, and outliers, where helium and neon concentrations make unreasonable jumps within a depth profile. These outliers were identified with two methods, the IQR (see appendix for an explanation) test and the Cooks Distance (see appendix for an explanation) test. As both tests are prone to distortion by extreme outliers, those data points identified by the test were manually evaluated and then judged. In total, the lower and the upper 0.5% of the data were classified as outliers. Even though some data was excluded, because of the reasons named above, Figure 4 still illustrates all sampling locations for transparency. Furthermore, in the salinity temperature analysis, samples that have not been measured for helium and neon are still included, and for the ΔHe and ΔNe analysis samples are still included that were neglected for GMW analysis. Therefore, even though there might

3.3 Temperature and Salinity Classification

Figure 5 illustrates absolute salinity vs. potential temperature to identify water masses in the study region. Most of the samples from the Ronne Front, particularly from the western end, were identified as HSSW (Figure 5, panels a and d). This makes sense, as the majority of sea ice production happens in this area, raising salinity levels (Paul et al. 2015). Also, it is logical that the HSSW samples primarily appeared in the datasets from 1995 and 2018, as the western end of the Ronne Ice Front was only reached during those years.

Many samples from regions (2), (3), and (4), which cover the Filchner Trough, show properties of ISW. This is reasonable, as most ISW leaves via the Filchner Trough towards the continental shelf break. A substantial part of the samples is indicated as WW. The majority of these WW samples (25-40% of each data set) are from the upper 400m, representing the general source water of the HSSW as described in the introduction. The remaining samples are a product of mixing between water masses, including water masses not indicated in the plot e.g., ASW as a less saline member and CDW as a warmer member.

3.4 Helium and Neon Excess Distribution

An overview of the spatial and temporal distribution of ΔHe and ΔNe with increasing water depth is presented in Figure 6. When comparing the different years, it is striking that ΔHe and ΔNe are on average 3 percentage points lower each in 1995 (Figure 6, panels a and b) and 2021 (Figure 6, panels j and k). This matches the lower 3S value given in Table 2 and hints at the same magnitude of helium and neon excess beyond the 3S value and atmospheric equilibrium over the whole time series.

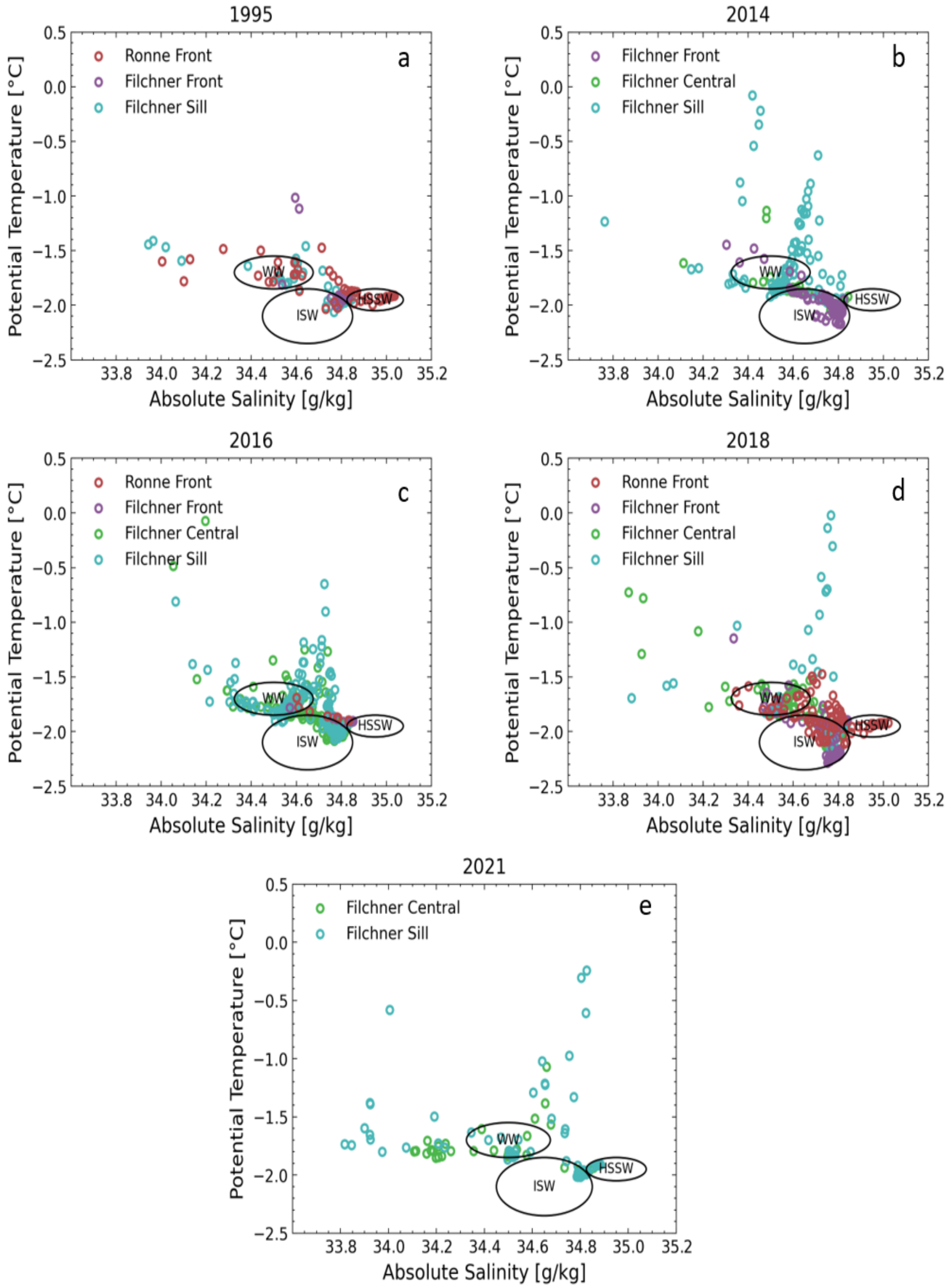

Figure 5: Absolute salinity vs. potential temperature for all years. Coloring is according to Figure 4, where the regions were given. Red is Ronne Front, purple is Filchner Front, green is Filchner Central, and blue is Filchner Sill. The ellipses indicate water masses.

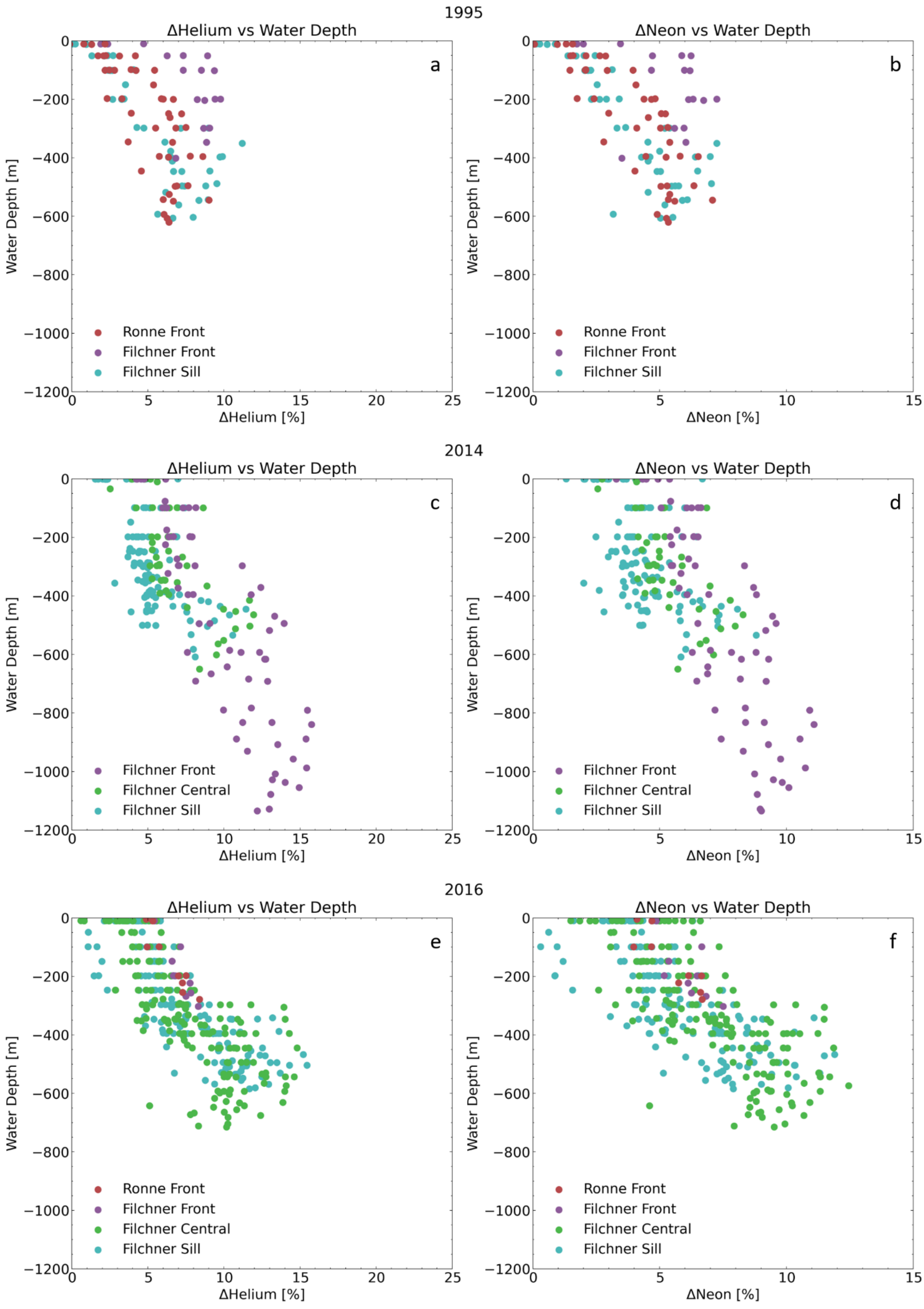

Figure 6: Overview of the observed ΔHe and ΔNe for all years. Coloring is according to Figure 4, where the regions were given. Red is Ronne Front (1), purple is Filchner Front (2), green is Filchner Central (3) and blue is Filchner Sill (4).

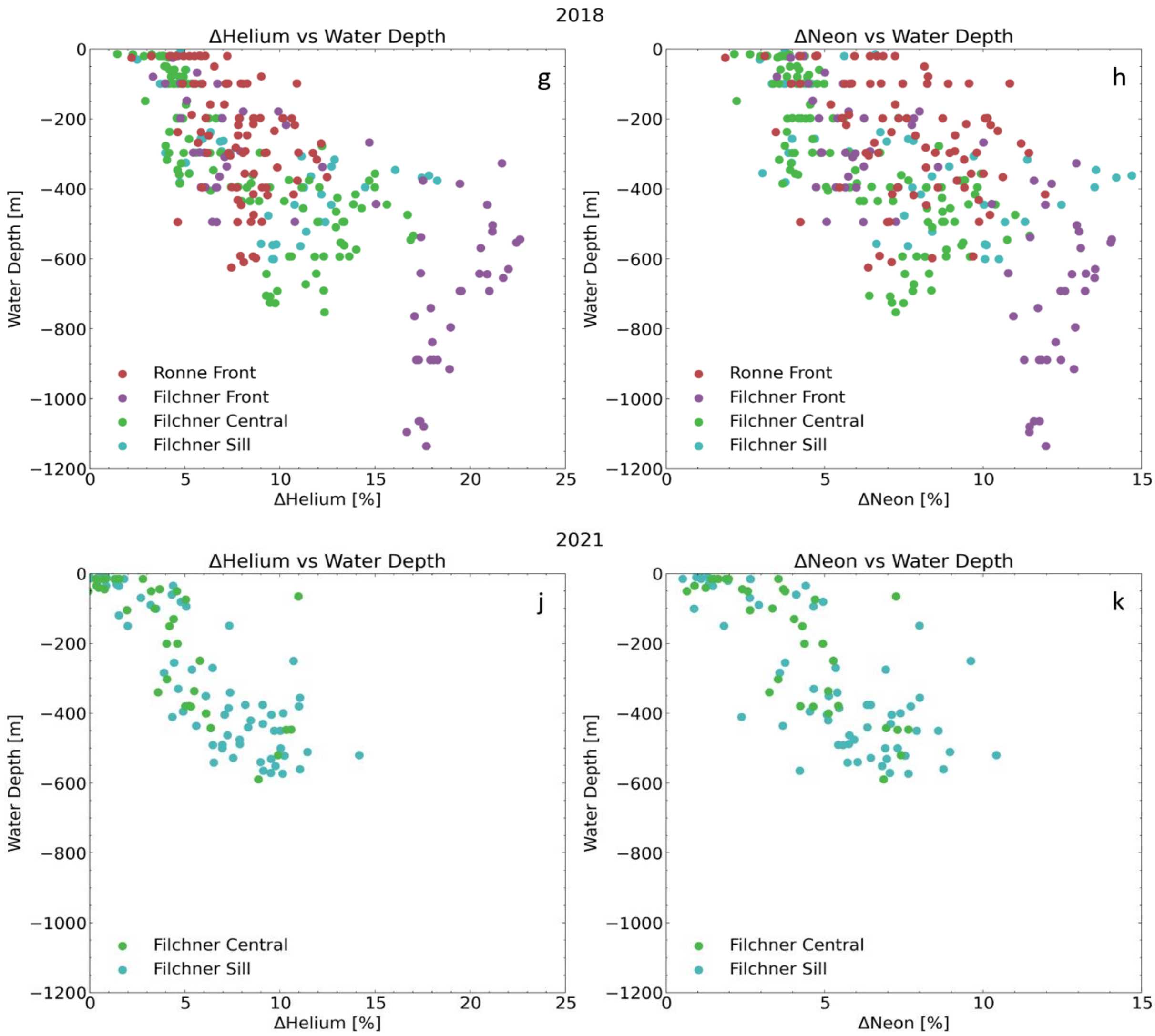

Figure 6 continues

Furthermore, the data show a general trend throughout all the years of increasing ΔHe and ΔNe with increasing depth. This observation aligns with the fact that ISW, which is formed by basal melting, is typically not found at the surface. Presumably, the ISW is likely also the reason the highest excesses throughout the datasets can be found in the region (2) because the main outflow of ISW from the FRIS cavity occurs through the Filchner Trough. With increasing distance from the ice shelf cavity dilution by mixing with other non-GMW enriched water masses takes place, resulting in lower ΔHe and ΔNe in regions (3) and (4). Due to scarce data this is, however, only supported by data from 2014 (Figure 6, panel c and d) and 2018 (Figure 6, panel g and h).

Another interesting feature is the high ΔNe values observed in 2018 in region (1) (Figure 6, panel h). High ΔNe values can be a result of sea ice formation, which is likely in region (1), and in line with the high salinities illustrated in Figure 5 (panel d). However, there are high salinities observed in region (1) in 1995, too (Figure 5, panel a), but with moderate ΔNe (Figure 6, panel b) and therefore no indications for sea ice formations, leaving this for discussion.

3.5 Basal Glacial Meltwater Fractions

The data points were projected onto a line to display the GMW fractions in a depth-over-distance plot. As previously mentioned, these lines are shown in Figure 4 in the methods section and are referred to as transects. A linear interpolation method was used between each data point to visualize the GMW distribution. The calculations were based on helium and neon individually and then the higher one was discarded to avoid overestimating GMW fractions by crustal helium or neon from sea ice formation. The bathymetry was derived from the International Bathymetric Chart of the Southern Ocean (IBCSO (Dorsch et al, 2022) DEM. It is important to note that the first transect, located closest to the ice shelf front, will comprise two regions, (1) and (2), whereas the other two only cover one region each, (3) and (4), respectively. Incorporating regions (1) and (2) into one transect was for a more practical representation of the depth-over-distance plot, without losing the distinctive differences based on their geographic location.

Figure 7-9 depict the distribution of GMW fractions across the different locations and years in the study area. High GMW fractions were observed in 2018 at the FIS front in depths of 500 – 1000 m with a maximum of 1.2% around 600 m (Figure 7, panel c). This is to be expected because this is where the ISW, not yet diluted, emerges from under the ice shelf. As described by Janout et al. (2021) the main pathway of the ISW is alongside the western flank of the Filcher Trough above the HSSW which is well visible in the figure, as the maximum of GMW is around 600 m and not at the sea floor. Because of an unfortunate lack of data, these relations are not visible in the other data sets. Yet, the area represented in the 1995 and 2014 data sets indicates the same order of magnitude of GMW fractions (Figure 7, panels a and b). If it had been possible to take samples directly in front of the FIS in the other years, the same ISW core might have been observed. However, Janout et al. (2021) reported different origination modes for the water flowing out from the FIS and hereby a possible different localization of the ISW core.

In the central region of the 2018 data set, there are two local maxima (0.8%) at both, the western and eastern flank of the Filchner Trough (Figure 8, panel c). This could be the continuation of the previously illustrated ISW core (Figure 7, panel c). Possibly the same continuation of the ISW at the western flank of the trough could be present in the 2016 data but cannot be displayed because of the lack of samples (depicted by missing black dots in Figure 8 and a resulting interpolation over a long distance). The other years lack even more data points to conclude about the central region.

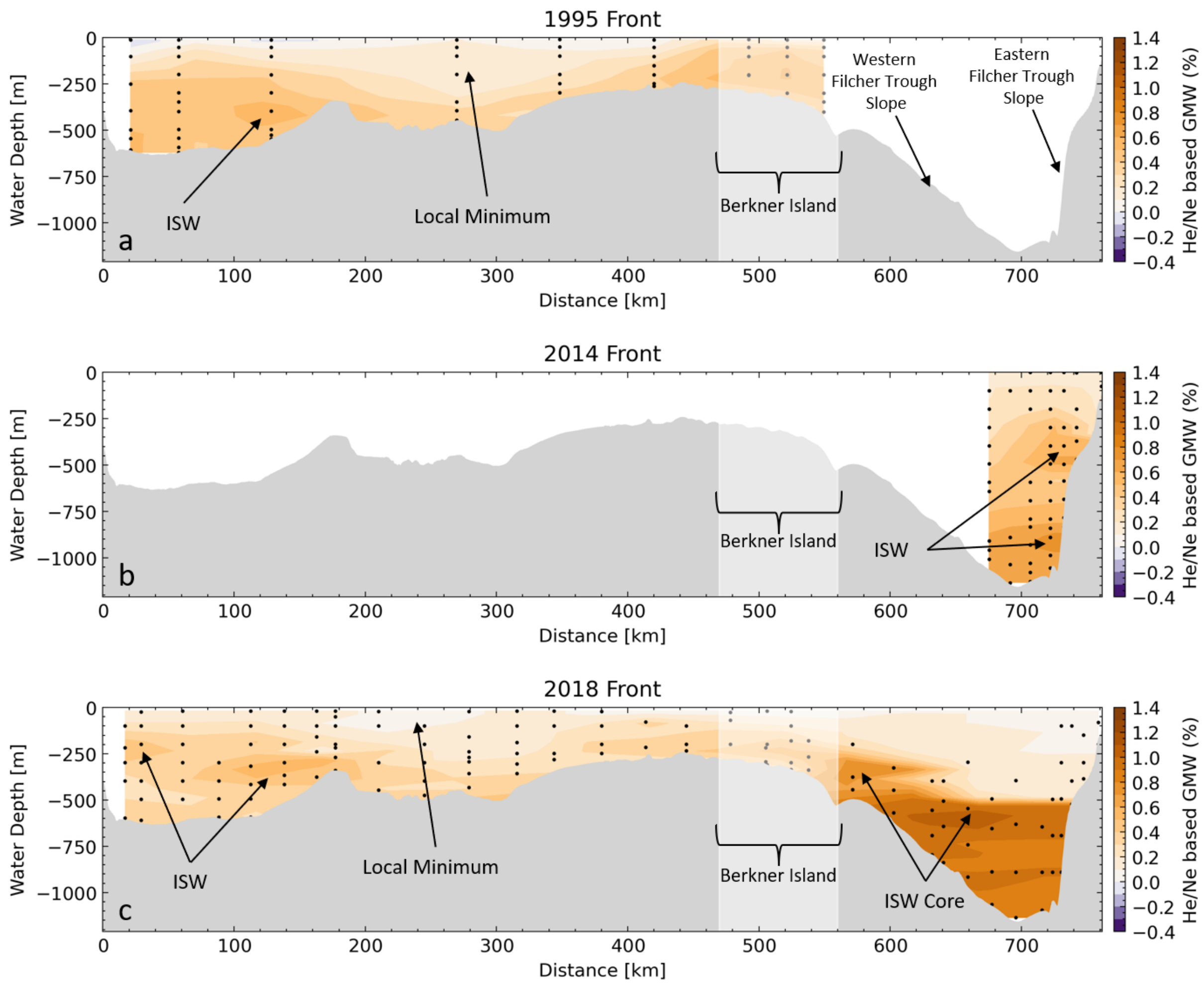

Figure 7: Illustrating GMW fractions in a depth-over-distance plot along transect 1 closest to the ice shelf front. This transect covers regions (1) and (2). The transparent area at the 500 km mark indicates Berkner Island. Region (1) Ronne Front is from zero to 500 km mark, region (2) Filchner Front from 500 km to 760 km. The color scale indicates the amount of GMW in %. Very prominent are the two ISW cores in the Filchner Trough in 2018, with the maximum observed value of 1.2% at a depth of approximately 600 meters (panel c). The ISW outflow in the Ronne Depression is also well indicated, both in 1995 and 2018 (panels a and c). Panel b shows that ISW was also observed in 2014, even though only half the Filchner Trough was sampled. Black dots indicate data points from samples.

Region 4, Filchner Sill is the only one that was sampled in all five years. Notably, the GMW fractions show the same magnitude across all years (Figure 9, all panels). The maximum is found in the 2018 dataset, reaching 0.8% (Figure 9, panel d). While the area with elevated GMW values has decreased considerably compared to the FIS Front, the magnitude has only slightly. The other years show similarly high values but in different locations. In 2021, the elevated values appear to be more widespread with two maxima, however, this might be due to missing data (as indicated by the absence of black points in Figure 9, panel a), leading to inaccurate interpolation. The consistent magnitude of GMW fractions, even far from the ice shelf, suggests continuous and relatively stable meltwater volumes, although the exact path of ISW is not traceable in every dataset.

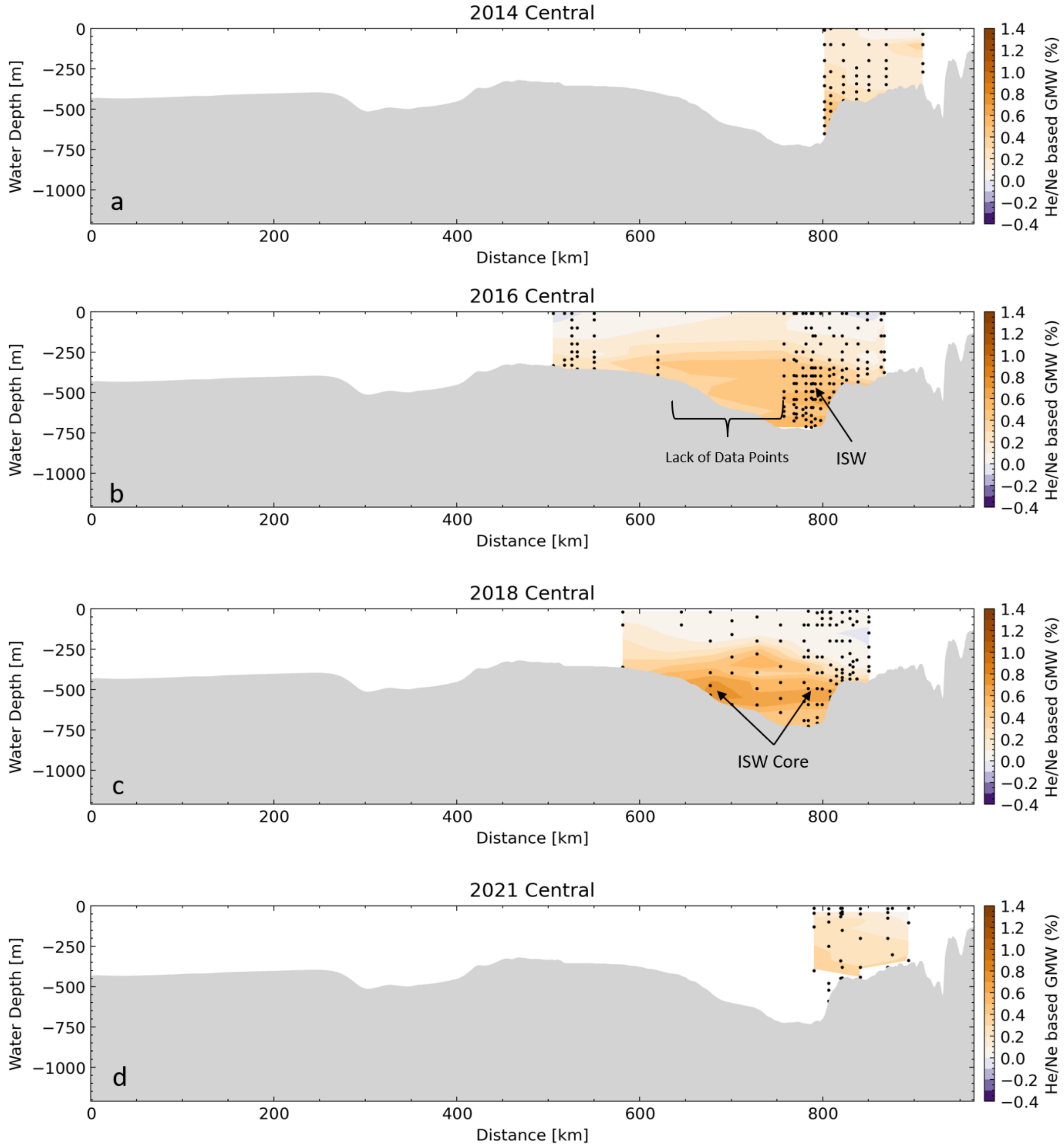

Figure 8: Illustrating GMW fractions in a depth-over-distance plot along transect 2. This transect covers region (3). The color scale indicates the amount of GMW in %. The ISW is especially prominent in 2018 (panel b) but is also visible in 2016 (panel a). In 1995 and 2021, the data is not sufficient to depict the ISW. In 2016 there is a big gap in data points, which might have caused inaccurate interpolation (panel b). Black dots indicate data points from samples.

In front of the RIS GMW fractions are moderate with the maximum at 0.7% visible in 1995 and 2018 at the 20-40 and 120-140 km mark (Figure 7, panels a and c). This suits the findings of Janout et al. (2021) who report indications of two ISW outflows in the Ronen Depression. At the 280 km mark seems to be a local minimum visible in both 1995 and 2018. A possible reason for this could be the inflow of mWDW as indicated in Figure 3. Similar to the Filchner Central Region in 2016, the density of sampling stations at the RIS Front in 1995 was low. Consequently, interpolation here was done over greater distances(>100 km), reducing the resolution. However, this is less of an issue in this case, as the changes, unlike those in the Filchner Trough, do not occur over such narrow geographic scales.

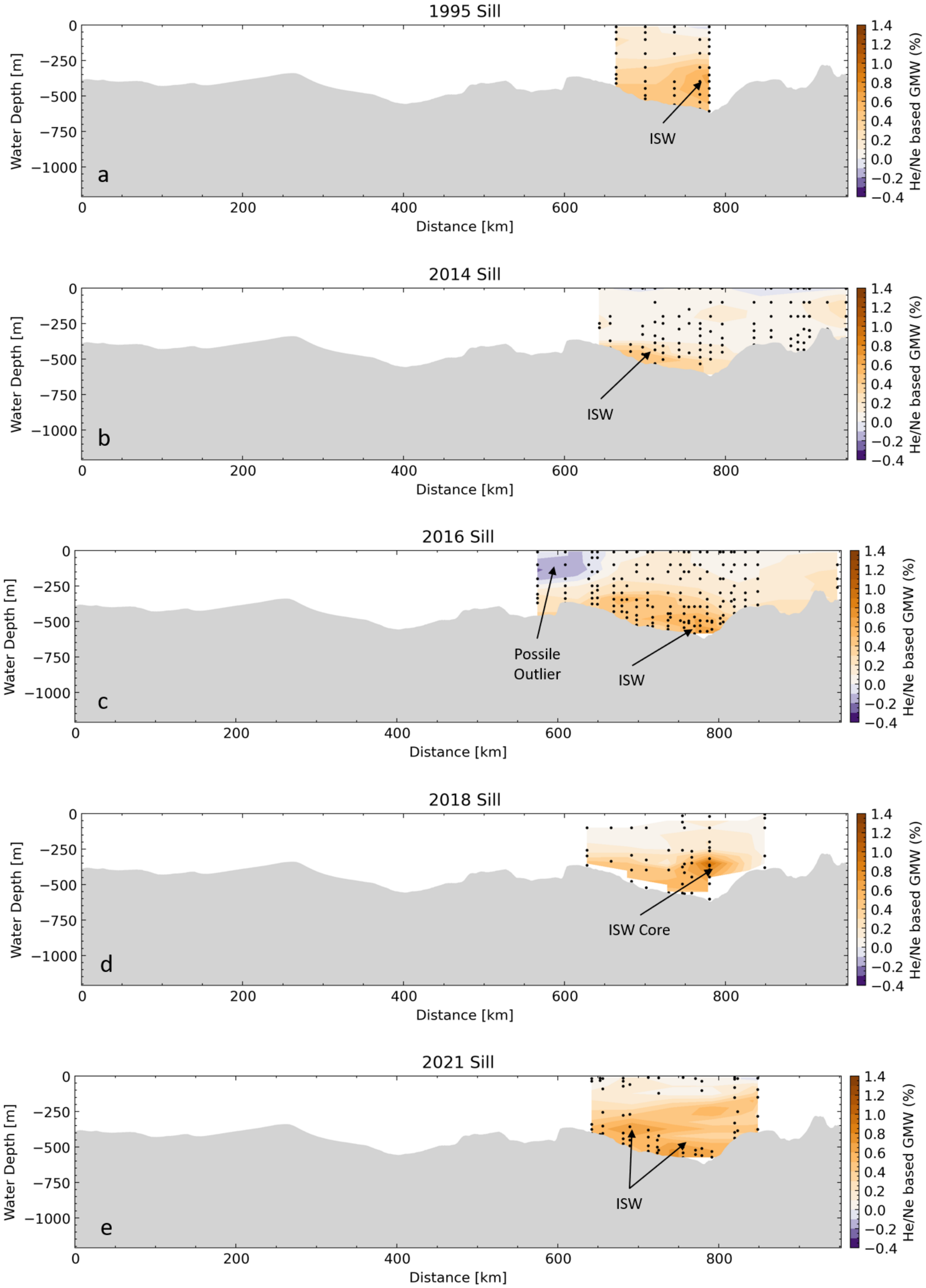

Figure 9: Illustrating GMW fractions in a depth-over-distance plot along transect 3 closest to the continental shelf break. This transect covers region (4). The color scale indicates the amount of GMW in %. The ISW is clearly visible in all years. Interestingly, in 2021 there are two local maxima (panel e). This is a feature unique to the 2018 data so far (Figure 7, panel c). Panel c indicates a possible outlier, as GMW fractions are below -0.2% here. Black dots indicate data points from samples.

Generally, GMW fractions are near zero at the surface in all regions and data sets. This is a logical consequence of the calculation method. The assumption was that no GMW was present in the upper 20 meters and the observed helium excess was used to determine the 3S value, which was then subtracted. Therefore, the result is zero GMW in the upper 20 meters. However, as the 3S value is an average applied to all samples, some surface samples show GMW fractions from -0.1- 0.1%. Except close to the continental shelf break in the 2016 data set, no results are below -0.2% (Figure 9, panel c). This strong negative value could be an outlier not identified by statistical methods before or the 3S value for 2016 is too high. Except for this global minimum, the overall positive results seem reasonable, as the seawater cannot contain less than zero percent meltwater.

3.6 Additional Helium and Neon Sources

Ideally, if there were no other sources of helium and neon, the calculated GMW should be the same for both gases. However, there were differences throughout all sets with a maximum of up to 0.3 percentage points suggesting the presence of additional sources. To tackle this problem, only the lower result of the GMW calculation of either helium or neon was used for each data point, as mentioned above. Nevertheless, these additional sources can affect the GMW and indications for it can be found in the data.

3.6.1 Crustal Helium

The amount of crustal helium contributed can be estimated and illustrated with a scatter plot of ΔHe vs. ΔNe (Figure 10). It should be noted that in Figure 10, the respective 3S values have not yet been subtracted from ΔHe and ΔNe, to avoid distorting the effects of crustal helium and sea ice formation. For this reason, some samples fall into a range with higher GMW fractions than shown in Figure 7-9. When the only source of helium and neon enrichment is melting, the data would scatter along a straight line from the origin to 1280% ΔHe and 890% ΔNe. In the crust below the ice sheet, α-decay can increase the amount of ^{4}He in the ice up to 4.5 times compared to pure meltwater (Craig & Scarsi, 1997; Jean-Baptiste et al., 2001). With 10% of GMW enriched by this level of crustal helium, the line shifts to 1728% He and 890% Ne.

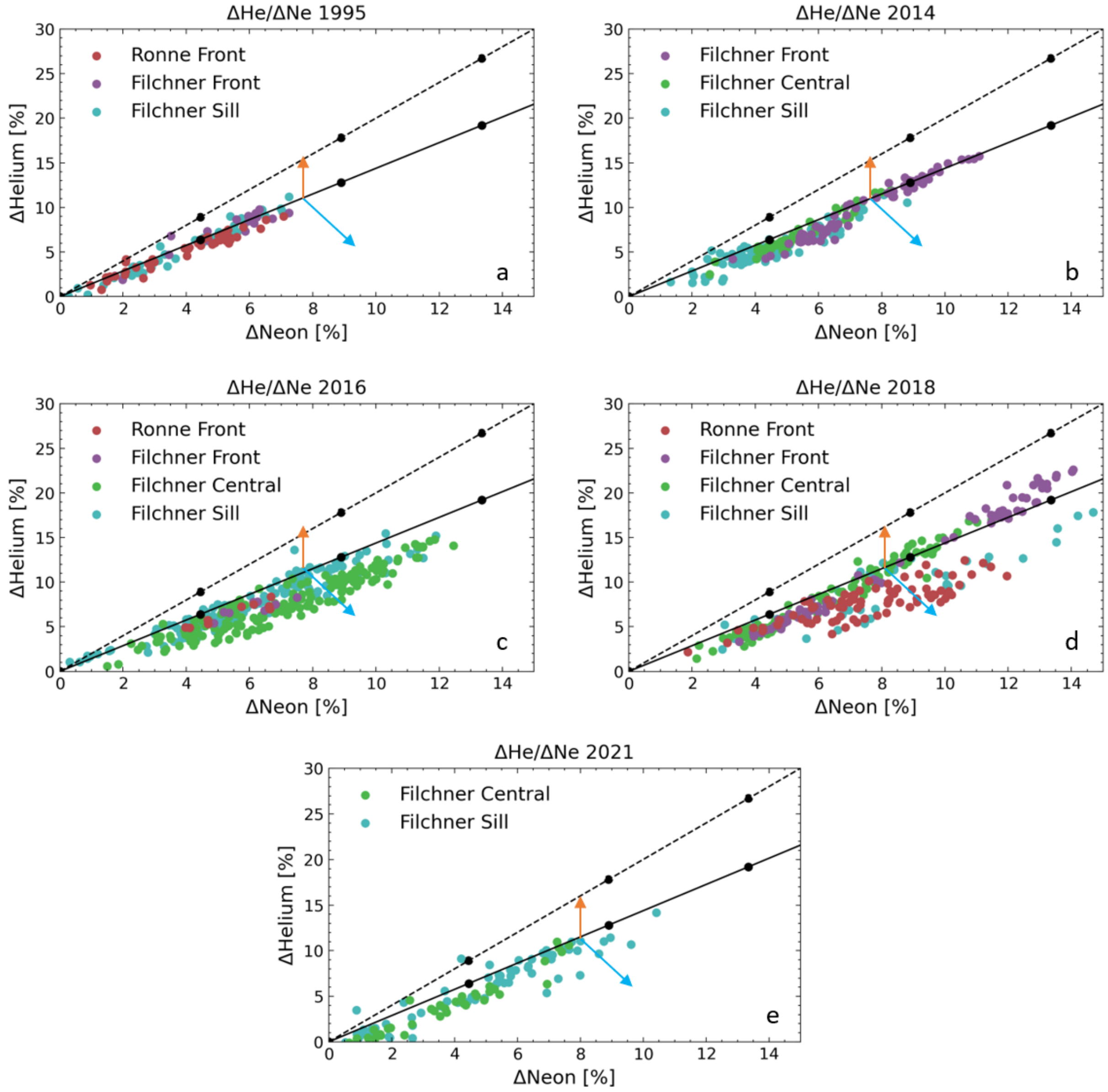

Figure 10: ΔHe vs. ΔNe for all years. The orange arrow points towards enrichment by crustal helium and the blue indicates sea ice formation. The black line indicates pure meltwater. The dashed black line depicts a combination of 90% pure GMW plus 10% crustal helium-enriched GMW with 4.5 times higher helium than pure GMW. The black dots denote steps of 0.5%. Only samples in front of the FIS in the 2018 (panel d) data set plot toward crustal He enrichment, while most others point towards sea ice formation.

It is primarily the samples from 2018, collected directly at the front of the FIS, that show a source of crustal helium, some of them close to the line of 10% enriched GMW (Figure 10, panel d). This is not surprising, as crustal helium can only be detected where meltwater is present. Since the 2018 samples from the FIS front show the presence of ISW most clearly and thus GMW, it logically follows that they also show a signal of crustal helium.

The hypothesis that the Filchner Trough is the primary outflow pathway for the ISW and that there is a source of crustal helium is supported by Figure 11. This figure shows Δ(He/Ne) along the same transects and regions as Figure 7 for GMW. The strong positive signals (above 2%) in the Filchner

Trough (regions (2), (3), and (4)) indicate the presence of additional crustal helium (Figure 11-13). The maximum Δ(He/Ne) of up to 8% in the 2018 dataset (Figure 11, panel c) corresponds to the location of the GMW maximum (at 600 meters above the eastern flank). Since crustal helium enrichment is only detectable where GMW is present, and a crustal helium source is evident, the same geographic and temporal patterns observed for GMW fractions apply. This suggests a continuation of the crustal helium signal in the Filchner Central region in both 2016 and 2018, which can be seen in Figure 12, panels b and c, respectively). In other datasets, crustal helium enrichment is less pronounced than in 2018 (Figure 11-13 with Δ(He/Ne) barely above 2%) and is difficult to quantify (Figure 10, panels a, b, c, and e, with samples close to the pure meltwater line). However, since a crustal helium signal is observed in the Filchner Sill region each year, even if just slightly above 2% Δ(He/Ne) (Figure 14), it is reasonable to assume it would also be detectable throughout the entire Filchner Trough. Yet, changes in melting location, rate, or meltwater pathway could have affected the amount and detection of crustal helium, highlighting the importance of comprehensive spatial and temporal sampling coverage.

3.6.2 Sea Ice Formation

Detecting a source of crustal helium and quantifying its contribution is relatively straightforward. However, assessing sea ice formation presents more challenges. The primary indicators for sea ice formation are ΔNe and salinity. Similar to crustal helium, ΔHe/ΔNe and Δ(He/Ne) plots can help identify samples affected by sea ice formation. Unfortunately, results vary across different indicators, complicating the drawing of clear conclusions. Additionally, only the residual water from which the ice was formed is observed, adding to the challenge. This residual water can be transported and observed at greater depths and distances from the formation zone. The following paragraph attempts to combine the different indicators for the various datasets and locations to assess the influence of sea ice formation on the samples. However, accurately estimating the amount of sea ice is more complex and will be elaborated on in detail in the discussion section.

The majority of the 2016 samples, along with the Filchner Sill and Ronne Front samples from 2018, indicate sea ice formation, as they plot clearly below the pure meltwater line in Figure 10 (panels c and d). While samples from the other years also plot below this line, they remain close to it, making it difficult to attribute these results solely to sea ice formation Figure 10 (panels a, b, and e).

In Figure 11-13, values below 0% Δ(He/Ne) suggest residual water from sea ice formation. This is most clearly observed in samples from the Ronne Front and the Filchner Sill in 2018 (Figure 11, panel c, and Figure 13, panel d), as well as from Filchner Central in 2016 (Figure 12, panel b). Notably, the large area of negative Δ(He/Ne) (up to -2%) at the Ronne front in 2018 is a unique feature of the entire time series

(Figure 11, panel c). Extensive areas with values below 0% Δ(He/Ne) are not evident in the other datasets, which is somewhat consistent with plotting close to the pure meltwater line in Figure 10.

The analysis of salinity and sample identifications from Figure 5 adds another layer of complexity. The 2018 Ronne Front samples were identified as HSSW (high salinity due to brine rejection), which is consistent with sea ice formation indicators (Figure 5, panel d). However, the 1995 Ronne Front samples, also classified as HSSW, do not match other indicators (Figure 5, panel a).

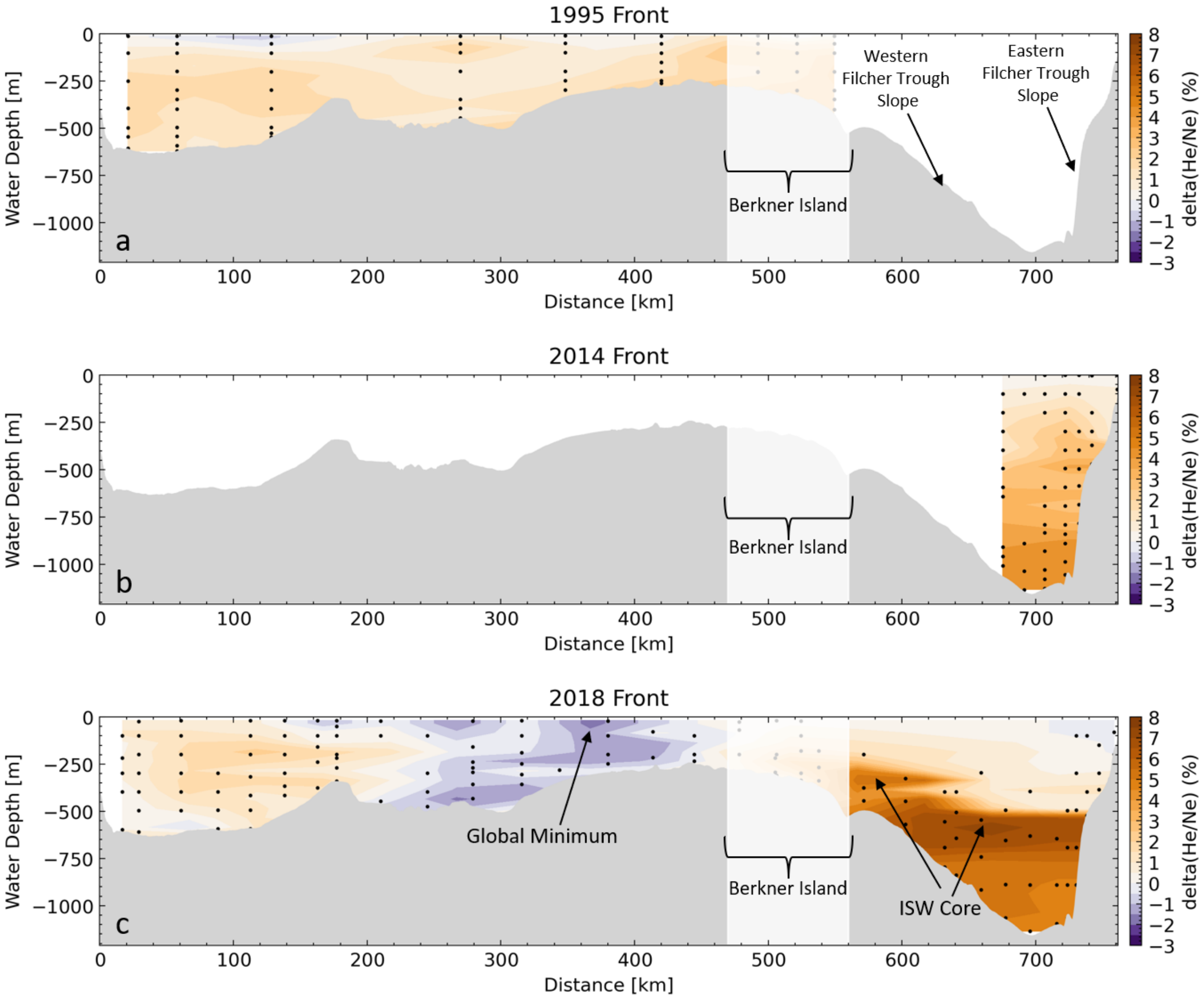

Figure 11: Illustrating Δ(He/Ne) in a depth-over-distance plot along transect 1 closest to the ice shelf front. This transect covers regions (1) and (2). The transparent area at the 500 km mark indicates Berkner Island. Region (1) Ronne Front is from zero to 500 km mark, region (2) Filchner Front from 500 km to 760 km. The global minimum of Δ(He/Ne) is seen in 2018 (panel c) and covers a large area. A clear influence of crustal helium is seen in 2018 (panel c), supporting the presence of ISW). Black dots indicate data points from samples.

Samples from 2014, 2016, and 2021 present additional complexities. Specifically, none of the 2014 and 2016 samples were classified as HSSW (Figure 5, panels b and c). While some 2021 samples show HSSW characteristics (Figure 5, panel e), 2014 and 2021 samples are close to the pure meltwater line in Figure 10 (panels b and e), but 2016 samples are not (panel c). Additionally, 2014 samples do not show significant negative Δ(He/Ne) in Figure 11-13, whereas 2016 samples show noticeable negative values, and 2021 samples display only minor negative values.

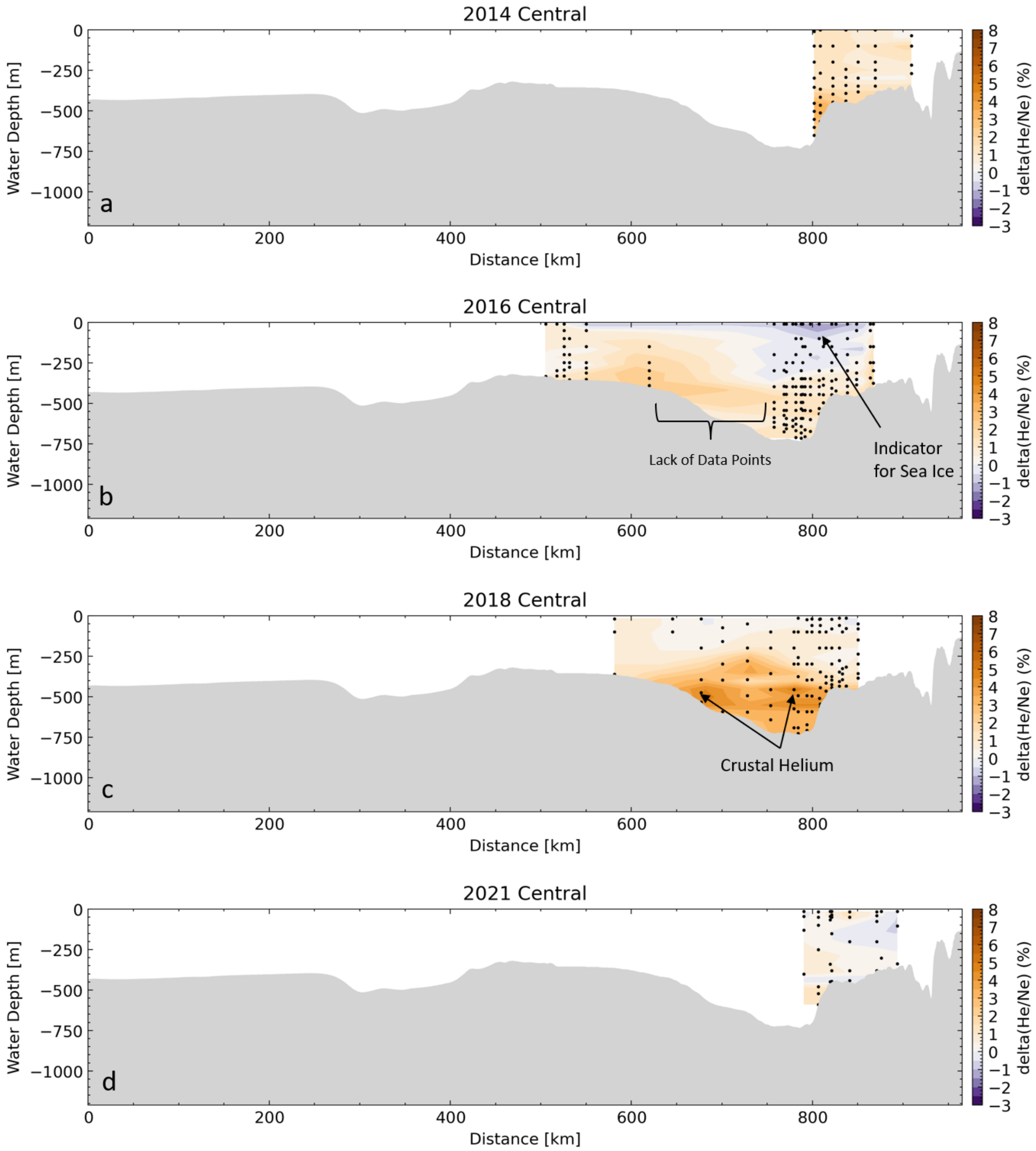

Figure 12: Illustrating Δ(He/Ne) in a depth-over-distance plot along transect 2. This transect covers region (3). The continuation of the crustal helium source can be seen in 2018 (panel c) indicated by values above 2% Δ(He/Ne). In 2016 there is a big gap in data points, which might have caused inaccurate interpolation (panel b). Black dots indicate data points from samples.

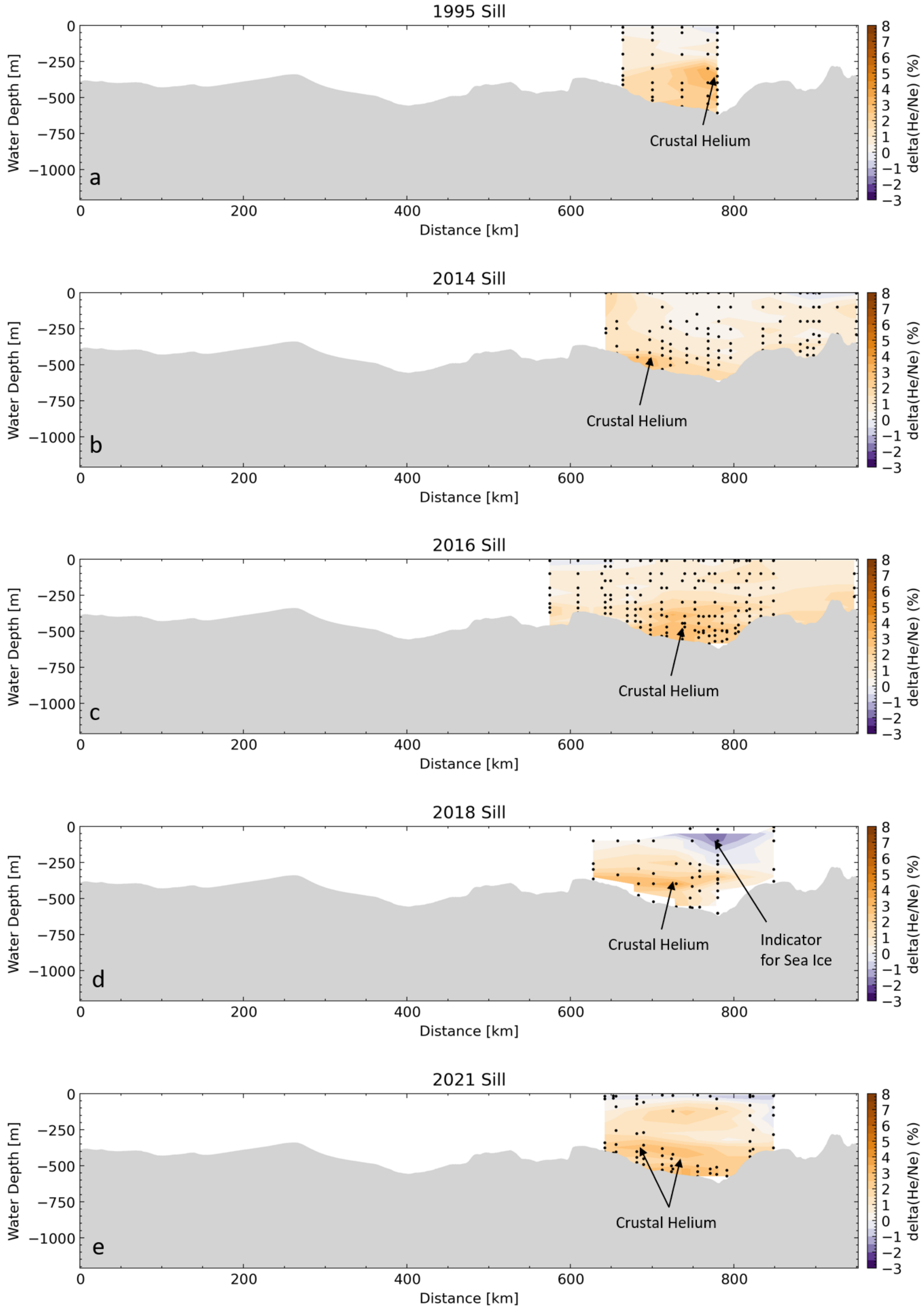

Figure 13: Illustrating Δ(He/Ne) in a depth-over-distance plot along transect 3 closest to the continental shelf break. This transect covers region (4). Residual water from sea ice formation is indicated in 2018 (panel d). In all other years, a signal of crustal helium enrichment is visible, indicated by values above 2% Δ(He/Ne). Black dots indicate data points from samples.

4. Discussion

The following section discusses the main findings and the associated challenges. One of the most significant factors is the determination of the 3S value and how it should be managed. This includes not only the physical processes influencing the 3S value but also potential deviations caused by the instruments used. The 3S value is closely linked to the calculation of GMW fractions as well as sea ice formation. Therefore, the discussion will follow this structure.

4.1 Surface Super Saturation 3S

The accurate quantification of GMW fractions in oceanographic studies using noble gases, specifically helium and neon requires, that all interfering factors that could alter their concentration be excluded before attributing the concentrations to pure GMW. Both gases have well-defined solubilities under atmospheric conditions (Weiss, 1971), allowing for the accurate estimation of equilibrium states. However, the natural background, influenced by dynamic oceanic processes such as bubble injection is challenging. Bubble injection occurs when breaking waves trap and dissolve small gas bubbles in the water, producing excess helium and neon that can mistakenly be attributed to GMW. Furthermore, errors of measurement and calibration have to be considered. Therefore, correcting these effects is crucial to receive meaningful results.

4.1.1 Challenges in Determining the 3S Value

The natural background level of noble gases, referred to as 3S, is affected by turbulent processes at the ocean surface, and assuming uniformity across larger regions (e.g., the whole Weddell Sea), or multiple years can lead to inaccuracies. This makes it necessary to determine the 3S from samples taken in spatial and temporal proximity to other samples that are analyzed for their GMW content. Due to the turbulent nature of oceanic processes, the determination of 3S should be based on a large number of samples collected from various stations at sufficient distances from the ice shelf front. This distance is necessary to avoid attributing helium and neon to the 3S value, which is in fact induced by GMW. In sufficient distance, the GMW baring water would have mixed enough with ambient water or other water masses and any detected helium and neon is induced by atmospheric equilibrium or bubble injection. In addition to the distance from the ice shelf, the water depth is important to realistically determine the 3S value. Samples from the upper twenty meters are ideal, as they are most likely to either resemble equilibrium with the atmosphere or the influence of bubble injection as result of the current air-ocean conditions.

Nevertheless, time, resources, and available sample containers often limit the number of samples that can be collected, especially in regions where sampling close to the ice shelf front is most desirable and therefore prioritized. Therefore, when lacking enough samples at a suitable distance to the ice shelf front, determining the 3S value can be approached differently. If samples are taken at the surface, close to the ice shelf front and GMW is present there, it would have been transported from deeper layers via upwelling of ISW. ISW is the main GMW-bearing water mass and has a higher density than WDW (or mWDW), the Weddell Sea derivate of CDW. Hence, the upwelling of ISW to the surface would also upwell a significant amount of CDW derivate. As briefly described in the methods, CDW is characterized by an excess of ^{3}He from hydrothermal vents and its δ^3He should be significantly higher than -1.8%. Antarctic surface samples though should be in equilibrium with the atmosphere and have a negative δ^3He of -1.8%. The conclusion is that if the surface samples show negative δ^3He close to -1.8% contamination with GMW can be excluded, as neither CDW (or mWDW in this case) nor ISW have been upwelled. Therefore, surface samples independently of their proximity to the ice shelf front are sufficient to determine whether helium and neon concentrations are influenced by upwelling or solely by bubble injection. Note, that this concept does only hold for helium-based 3S calculation. In the upper 20 meters, neon may be influenced by sea ice formation, independent of the proximity to the ice shelf. As a result, the 3S value for neon should always be derived based on the correlation given by Loose & Jenkins (2014), as described in the methods.

The relationships discussed above apply to all samples used to calculate the 3S values in this study. For example, samples from the upper 20 meters of water, irrespective of their proximity to the ice shelf, were considered based on the assumption that surface water is generally unaffected by GMW (showing δ^3He ratios in the order of -1.8%).

4.1.2 Natural Variability and Methodological Robustness

The data suggest a multi-annual variability in the 3S value (Table 2) with a maximum difference as high as 0.06 nmol/kg helium between 2018 (max) and 1995 (min). This leads to the question: Is the observed variability of the 3S value due to actual changes induced by bubble injection or measurement or calibration inaccuracies over time?

For comparison other data sets from 1990, 1991, 1992, 1996, 1998, 2004, 2006, 2008, 2010, and 2013 were looked at too, and reveal a significant variation in 3S values, with differences of up to 3 percentage points between years (Figure 14). Most of this data originates from the Weddell Sea too, but not from the vicinity of the FRIS (FRIS samples are highlighted in orange). For this reason, they were not analyzed in detail, as they do not fit the scope of this work, but give an overview of the variability of the calculated 3S value. In those data, a broader range of 0.5% to 4.6% for helium could be calculated. Despite these variations, a pattern is evident, with values clustering around 1-2% or 4%, with a margin of ±0.5%. On the contrary, identifying a temporal variability pattern based on the data shown in Figure 14 seems unfeasible. All data shown in Figure 14 are from austral summer (except from 2006 data which was obtained during winter season). Hence a seasonal variability can hardly explain the variability in the 3S values. Further, clear jumps in the height of the 3S values, even from those not taken near the FRIS, indicate that a geographical dependence on the 3S value is rather unlikely.

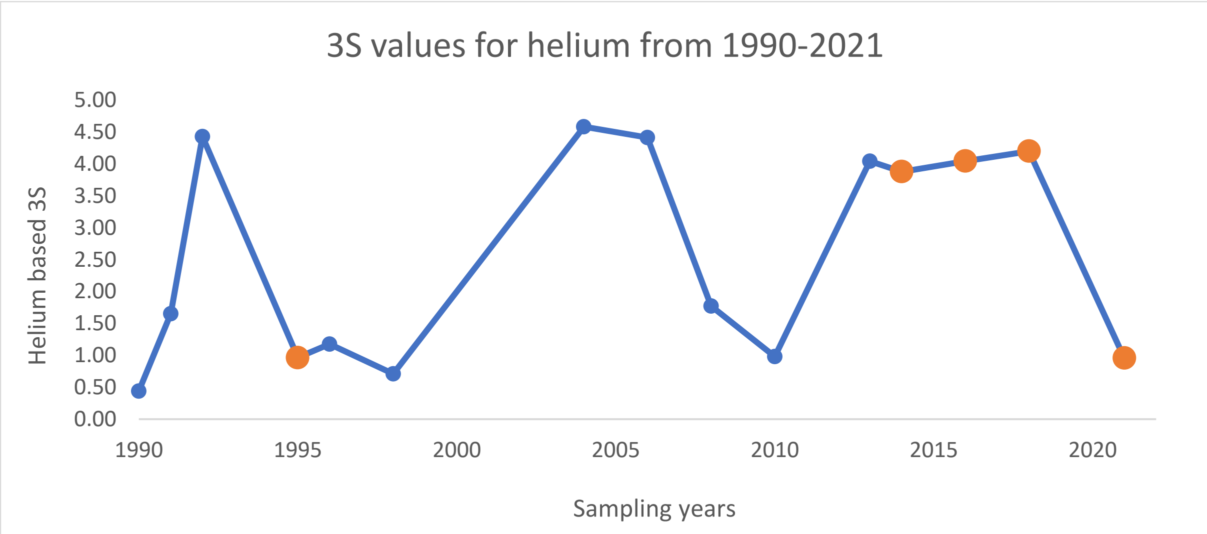

Figure 14: 3S values for helium from samples in fifteen different expeditions. Orange dots represent the data analyzed in detail in this work and, therefore, take in the vicinity of the FRIS. There is a prominent variability over the entire recorded period, hence the variability is most likely not connected to geographical differences.

The trace gas measurements were conducted at IUP Bremen, with data spanning nearly three decades. Over this period, the calibration standards used in analyses were self-made (and cross-calibrated to a historic super-standard) (Sültenfuß et al., 2009), which introduces potential variations due to changes in instrumentation or standard production processes. Factors such as decreasing pressure in gas cylinders as they empty could affect the actual amount of gas extracted, contributing to measurement uncertainties. To address these challenges, the 3S value was individually determined for each data set in this study, instead of applying a single literature value across multiple datasets (as done in Mareike Berghald, 2021). Two scenarios are possible for the calculated variability of the 3S value:

Scenario 1: The natural background changes within a few years. The measurement method is either robust and resembles the annual changes accurately, or it introduces systematic deviations due to miss-calculated standards, though these deviations are not large enough to obscure the variability.

Scenario 2: The natural background is relatively stable over decades. In this case, the measurement method introduces a high order of systematic deviations, resulting in apparent annual changes.

Given the history of this method (Schlosser, 1986), the constant operation at the IUP since 1989 (Sültenfuß et al., 2009), and the overall robustness of mass spectrometry, it is highly doubtable that measurement-induced uncertainties are of such a distorting order, as depicted in scenario 2. Therefore, an annual variability in the natural background is a realistic case.

4.1.3 Implications on GMW Fractions

Whereas the variability of the natural background can be regarded as proven, the calculated 3S value might still be affected by small systematic measurement errors. However, all samples from a corresponding year were analyzed during the same respective measurement run. Hence, it can be assumed that the same order of uncertainties was applied to all samples within a given set respectively. During the GMW calculation process, the 3S value is subtracted and hereby a potential systematic measurement error too. Therefore, the results of the GMW calculation are compensated for measurement-induced uncertainties and uncertainties of the 3S value. This makes the results of the GMW analysis meaningful, as consistent results over time indicate a reliable method despite natural variability and methodological uncertainties, given the 3S value is determined for each data set individually.

Nevertheless, the approach of the individual 3S value raises questions about its applicability to all samples from a given year, regardless of the depth at which they were collected. This issue arises because of the transit times of water beneath the ice shelf. Nicholls & Østerhus (2004) suggest that the fastest pathway of HSSW under the FRIS takes 2 years, with indirect routes taking up to 6 years. Janout et al. (2021) confirm these findings. If a 3S value is determined based on surface samples from a particular year and then applied to ISW samples taken in the same year, the fractions of GMW could be over- or underestimated. Upon closer examination, this becomes a critical issue, as no ISW sample will reflect the conditions of surface samples from the same year because of the different formation times. However, no significant negative results have been computed, except for the Filchner Sill Region in 2016, which might be because of undetected outliers. This shows, that the chosen 3S values have not been overestimated. Yet, they could have been underestimated resulting in too high GMW fractions. Still, the consistency of the results throughout the entire time series strongly supports the stability of the meltwater fractions over the years.

This is conflicting and highlights the importance of a constant, if not annual monitoring of the Weddell Sea and a uniform method in determining the 3S value. Furthermore, multiple authors (Deike and

Melville, 2018; Kanwisher, 1963; Woolf, 1997) describe how bubble injection controls the uptake of less soluble gases in seawater and highlight the role of wind forcing. Historical wind data in combination with the data presented in Figure 14 could pose useful results regarding spatial and temporal patterns of the natural background. Therefore, a detailed assessment of the 3S value is linked to an in-depth study of wind conditions in the Weddell Sea, which at least goes beyond the scope of this work.

4.2 Basal Glacial Meltwater

In this work, the primary focus is on the quantification of GMW over a multi-decadal time series. ISW is less saline and colder, compared to its HSSW source, induced by the addition of GMW. Consequently, large-scale analysis of GMW fractions should focus on the ISW outflow zones. As previously described, ISW is observed at two sites, the Filchner Trough and the Ronne Depression (Figure 3). Initial observations suggest that GMW fractions have remained relatively stable over the past three decades, with a maximum of 1.2% in the Filchner Trough and 0.7% in the Ronne Depression, both computed from samples taken in 2018 (Figure 7, panel c).

4.2.1 Filchner Ice Shelf GMW

Unfortunately, only in 2018 was the complete FIS front sampled in such spatial resolution, therefore, the amount of GMW directly in front of the FIS during the other years can only be assumed. With increasing distance from the FIS front towards the continental shelf break, data from additional years is available for differentiation. Nevertheless, this data is also spatially restricted, does not always cover the complete width of the Filchner Trough, and is in some cases interpolated over large distances (>150 km, e. g. regions 3 and 4 in 2016 in Figure 7, panel a). Therefore, the exact comparison between multiple years stays assumptive. Yet, the results clearly show that the magnitude of the GMW fractions is consistent across all years.

Huhn et al. (2018) used samples from directly below the FIS, retrieved from sampling sites close (~50–65 km) to the front of the FIS in austral summer 2016/2017 and another location ~300 km farther south on the FIS in austral summer 2015/2016 (see their Figure 1). Their results are also based on noble gas analysis and were computed using the same calculation method described in this work. The highest GMW fractions they found were directly beneath the ice shelf base at the sampling sites close to the ice shelf front and were as high as 3.6%. Towards the bottom, the GMW fractions decreased but stayed above 0.5%. No data analyzed in this study shows GMW fractions above 1.2% contrasting their results. However, Huhn et al. (2018) explain the maximum they found by the absence of a mixed layer directly below the ice shelf base and therefore might be a locally limited snapshot. They also state that a substantial fraction (0.8- 2.7%) of water has refrozen on its pathway along the ice shelf underside and conclude that the mean GMW fractions beneath the FIS are 1.3±0.7%. Even though this is a significant uncertainty, their results still match GMW fractions computed in this work from the 2018 data set (Figure 7, panel c). Yet, comparing data from samples taken within the ice shelf cavity with those taken in front of the ice shelf is complex because of the variability in environmental conditions and physical processes as mixing with ambient water masses, refreezing, etc., affecting each location.

Huhn et al. (2018) also report GMW fractions from samples taken in open water close to the FIS front in 2014. These samples are the same as those referred to as 2014 and used in this study (Table 1). The calculation by Huhn et al. (2018) yielded only slightly lower results (<0.6%) compared to this work (<0.8%) (Figure 8, panel b). Because identical data and the same calculation method were used in this study, the differing results demonstrate different approaches to identifying outliers and determining the 3S value rather than varying outcomes (e. g. the 3S value in this study was smaller, resulting in higher helium and neon excesses to be attributed to basal melting).

A different method to assess GMW fractions was used by Akhoudas et al. (2020). Based on stable oxygen isotopes, they computed GMW fractions of up to 0.4% from samples taken in front of the FIS in early 2017. This is about a third of the results from the 2018 data (1.2%) and half from the 2014 data (0.8%) calculated in this study (Figure 7, panels b and c, respectively). Possible explanations for these significant differences could be the calculation method (oxygen isotopes vs. noble gases) or actual changed conditions between the sampling years (2014, 2017, and 2018). However, Akhoudas et al. (2020) compare their results to those of Huhn et al. (2018) and conclude concordance (0.4% and 0.6% respectively). This seems reasonable, as their results differ only by 0.2 percentage points. Interestingly, Akhoudas et al. (2020) even state the consistency of their results with those from the sub-ice shelf samples analyzed by Huhn et al. (2018), but do not deliver a detailed explanation.

This leaves a paradoxical situation for assessing GMW fractions at the FIS, as the results of both, this work and Akhoudas et al. (2020) contrast each other but seem to be in line with the results from Huhn et al. (2018) individually. A potential explanation could be the findings of Janout et al. (2021). They revisited noble gas data from 1995 and 2018 (identical to this study (Table 1)), investigated historical CTD data collected between 1973 and 2018, and brought this into a decadal context, including a discussion of the results from Huhn et al. (2018) and Akhoudas et al. (2020).

Based on the noble gas data from 2018 Janout et al. (2021) computed GMW fractions as high as 1% in the coldest and 0.6-0.9% in the reaming ISW along the FIS front, which is in agreement with the results of this study (1.2±0.1% and 0.7-1±0.1% respectively). Similar to the reasoning above, these differences are based on outlier identification and 3S value determination. Despite quantitative and temporal differences, the authors argue that their results are consistent with those reported by

Huhn et al. (2018) and Akhoudas et al. (2020). They link the coherence of these results to different modes that control the origin of the water masses in the Filchner Trough. These hydrographic conditions are called Ronne-mode and Berkner-mode and describe where the source HSSW originates from, and where most basal melting presumably took place.

4.2.2 Ronne-Mode and Berkner-Mode

Janout et al. (2021) explain that during the Ronne-mode, enhanced sea ice production by surface forcing (air-sea heat flux, wind, and water column structure) in front of the RIS results in a stronger inflow of HSSW in the Ronne Depression. The Ronne-HSSW fuels the circulation underneath the FRIS and brings heat which is available for basal melting underneath the RIS. In this case, the ISW outflow in the Filchner Trough is dominated by a source of Ronne-HSSW, and elevated GMW fractions at greater depths. The depth-related GMW increase is due to enhanced melting in the deeper cavity and flushing out of old water.

During Berkner-mode, sea ice production in front of the RIS is low and Berkner-HSSW is the main source of the ISW in the Filchner Trough. According to Janout et al. (2021) and Hattermann (2021) basal melting in Berkner-mode is characterized by less melting in the deeper cavity and enhanced melting close to the front of the FIS, resulting in more GMW at shallower depths.

Janout et al. (2021) observed that the conditions at the Filchner Ice Shelf (FIS) between 2014 and 2018 are best explained by a shift from a Berkner-mode to a Ronne-mode. Consequently, samples from 2014-2017, analyzed in detail by Akhoudas et al. (2020) and Huhn et al. (2018), reflect a Berkner-mode, characterized by low GMW fractions at the bottom of the Filchner Trough and high GMW fractions at the base of the FIS. In contrast, 2018 samples indicate a Ronne-mode, with higher ISW outflow and increased GMW fractions throughout the Filchner Trough. This shift is supported by calculations of sea ice production anomalies in front of the RIS from 1985 to 2017 (see Figure 12 in Janout et al., 2021), also indicating an active Ronne-mode in 1995 and a Berkner-mode from 2010-2017. However, data from 2014 and 2016 analyzed in this study likely represent a Berkner-mode but lack sufficient samples from key locations for confirmation. Recent findings by Stulic et al. (2023) align with Janout et al. (2018) in supporting these sea ice calculations. Additionally, Purich and Doddridge (2023) provide an analysis of overall Antarctic sea ice extent over a 44-year period, which initially appears to contrast with Janout et al. (2018) and Stulic et al. (2023), particularly for the years 2008-2015. However, since Purich and Doddridge (2023) focus on the entire Antarctic sea ice, their findings do not necessarily rule out increased sea ice formation at the RIS front. Janout et al. (2021), Hattermann (2021), Stulic et al. (2023), and Purich and Doddridge (2023) all emphasize the influence of the Southern Annual Mode (SAM) and the position of the Amundsen Low on sea ice formation. This highlights the need for a detailed study of wind patterns in the Weddell Sea, as such research is crucial for understanding the annual variability of the 3S value and a more accurate assessment of the transitions between Berkner- and Ronne-mode.

4.2.3 Ronne Ice Shelf GMW

Noble gas data from the Ronne Depression, the second noteworthy outflow of ISW, only exists from 2018 and 1995. Similar to the situation along the FIS front, the spatial resolution of sampling sites is remarkably better in the 2018 data set compared to 1995. Yet, they depict nearly identical conditions with GMW maxima of 0.7% and 0.6% respectively (Figure 7, panels a and c). Janout et al. (2021) reported GMW fractions of 0.7% and 0.5% in the Ronne Depression in 2018 and 1995 respectively. The similarity is not surprising because of the reasons discussed already (identical data, same calculation method, different 3S values).

The production of HSSW at the RIS front, driven by sea ice formation, acts as a controlling factor in regulating the circulation beneath the FRIS. This, in turn, significantly influences basal melting processes. Consequently, the RIS front is a critical component in shaping the hydrographic dynamics of the Weddell Sea. Therefore, it would be desirable to collect comprehensive data in this region for future analysis.

Huhn et al. (2018), Janout et al. (2021) and this study used the same calculation method and partially identical data, yet yielded slightly different results. These small differences are within the error margin of this work (±0.1%). Therefore, all results can be considered consistent, but it again emphasizes the consequences of data pre-treatment and further analysis (e. g. outlier identification and 3S determination).

4.3 Additional Helium and Neon Sources

4.3.1 Crustal Helium

A portion of the measured helium can be attributed to additional ^{4}He from alpha decay in the Earth's crust, which accumulates over geological time scales in the lower layers of the ice sheet (Bieri et al., 1964; Craig & Scarsi, 1997; Suess & Wänke, 1963). Either by basal melting or geothermal heat and friction on land, this helium is released and added to the meltwater. Because helium concentration measurements cannot distinguish between different sources, an alternative approach is necessary to avoid overestimating GMW fractions. This issue was addressed by selecting the lowest calculated GMW value based on either helium or neon measurements. Despite this, estimating the amount of ^{4}He is meaningful, as it could be used to understand ice-sheet dynamics, ocean circulation, and the influence of geological processes on the ocean.

Huhn et al. (2018) identified a crustal helium source with up to 13% ^{4}He enriched meltwater. The authors attribute it to the nearby Support Force Glacier (SFG), one of the primary contributors to the FIS. The current study shows a crustal helium enrichment of about 7% (Figure 10, panel d), with sporadic samples reaching 10% (panels a, b, and e). Considering that samples analyzed by Huhn et al. (2018) were taken directly under the ice shelf, while this study's samples were taken in front of it, these differences are plausible. Another explanation for the differences would be the shift from Ronne-mode to Berkner-mode as previously discussed. Yet, the effect of changing modes is unfeasible to assess because the comparable data in this study is from 2014 and 2016, years in which a comprehensive sampling of the relevant location (FIS front) was not possible. Nevertheless, all years exhibit a crustal helium signal in region (4) (Figure 13), and despite not being directly comparable to the results of Huhn et al. (2018), they align their findings. Furthermore, the effects of crustal helium and sea ice formation on the helium and neon concentrations can balance each other and would not be visible in $\Delta He/\Delta Ne$ and $\Delta(He/Ne)$ plots. Both figures become most meaningful under the assumption, that the effect of crustal helium and sea ice formation is bound to the sampling location. This means, that samples identified as ISW are only affected by crustal helium, whereas only samples from the surface are affected by sea ice formation. Janout et al. (2021), focused solely on neon data and forego the need to discuss the effect of crustal helium influence.

4.3.2 Sea Ice Formation

As elaborated on in the results section, the different indicators for sea ice formation are very contrasting over the time series. Therefore, assessing spatial and temporal differences in sea ice formation based on salinity and noble gasses stays conflicting. To assess this a more detailed study would need to be conducted, focusing on the individual effects. However, his is behind the frame of this thesis.

Quantifying sea ice formation remains challenging too and is usually done by modeling, based on satellite data. Drucker et al. (2011), Haid and Timmermann (2013), Nihashi and Ohisima (2015), Paul et al. (2015), Janout et al. (2021), and Stulic et al. (2023) attempted this and used varying input and assumptions. Although, extensive modeling is beyond the extent of this study, a broad estimation using noble gases can be given, following the approach of Huhn et al. (2021b) and Hahm et al. (2004). These authors assessed sea ice formation based on sea ice/seawater partition coefficients of helium and neon, first determined by Postlethwaite (2002).

The maximum neon concentration relative to the 3S value was determined for the upper 100 meters of water and applied to the formula of Huhn et al. (2021b) (see their equation 3), to calculate the fraction of frozen water. The resulting sea ice thickness was derived assuming water and ice densities of 1025 kg/m³ and 900 kg/m³ respectively. Combined annual polynya areas estimated by Paul et al. (2015) were used to compute the volume of sea ice production (see abbreviations RO, IB, and FI in their figure 1 and table 1). Table 3 presents the maximum neon differences, frozen water fractions, resulting sea ice thicknesses, and corresponding sea ice volumes for each analyzed dataset.

Year	Max. Ne diff. [%]	Fraction of frozen water [%]	Sea ice thickness [m]	Sea ice volume [km³]
1995	5.6	16	18	90
2014	3.7	10	12	61
2016	4.1	12	13	67
2018	5.5	15	17	88
2021	4.0	11	13	65

Table 3: Maximum neon differences, frozen water fractions, resulting sea ice thicknesses, and corresponding sea ice volumes.

Comparing these results with other studies is challenging because of differences in methodologies, assumptions, and available time series, which result in varying outcomes and large uncertainties. For example, reported values for just the RIS range from 29 km³ (Paul et al., 2015) to 96 km³ (Janout et al., 2021), with other studies reporting 42 km³ (Haid and Timmermann, 2013; Nihashi and Ohisima, 2015), 44-52 km³ (Stulic et al., 2023), and 90 km³ (Drucker et al., 2011). The assumptions in this study may also introduce potential errors. Neon concentrations, although collected at only a few locations, were sometimes averaged over large distances. Additionally, this study considered the entire area in front of the FRIS, whereas the results given in the works named above are solely from the RIS. A more precise analysis and detailed comparison with other studies would exceed the scope of this work and is therefore not approached. However, the results fall within the expected ranges, suggesting that with comprehensive data and further investigation, noble gases could be a valuable comparison tool.

5. Conclusion and Summary

The objective of this thesis was to investigate and quantify GMW fractions from the FRIS using noble gas data collected over the past three decades. Helium and neon were identified as effective tracers for estimating GMW. The results indicate generally stable conditions across all analyzed datasets, with the largest GMW amounts (1.2±0.1%) found in the Filchner Trough at a depth of 600m from 2018 samples. The Filchner Trough is confirmed as the main outflow of ISW, which carries the GMW. The Ronne Depression also serves as a significant ISW outflow, with GMW maxima of 7±0.1% observed in samples from 1995 and 2018.

While other studies (Huhn, 2018; Janout, 2021; Akhoundas, 2020) have used similar data and methods, differences in their results compared to this work can be attributed to variations in sampling locations and prevailing conditions. For instance, Janout (2021) highlights that different circulation modes, such as Berkner-mode and Ronne-mode, can influence ISW outflows and the location and extent of melting.

A key finding of this research is the importance of accurately determining the natural background, specifically the 3S value, which appears to be highly variable with annual changes. Precise determination of this value is crucial to avoid over- or underestimating GMW fractions. However, suitable data for determining the 3S value are not always available. This thesis proposes an approach where the 3S value for helium is averaged from all available samples in the upper 20 meters, based on the assumption that no GMW is present. This assumption is validated by the δ3He ratio of the analyzed samples, which aligns with the expected ratio of -1.8 in Antarctic surface water.

There were limitations in comparing the data analyzed in this study with that of other researchers, primarily due to the inconsistent sampling resolution across different years. A more extensive monitoring program, sampling regions comprehensively on an annual basis, would be beneficial for assessing the future stability of the FRIS and for more accurate 3S value calculations. Additionally, a detailed study of wind patterns could provide insights, as wind influences both the 3S value and sea ice formation, which in turn affects circulation and GMW fractions.

Noble gases have proven to be a reliable method for computing GMW fractions, providing results consistent with other techniques. They are also suitable for estimating sea ice production, although this approach needs to be refined. Some researchers have suggested that the FRIS could collapse if mWDW penetrates the ice shelf in larger quantities. This study, however, has found that GMW fractions have remained stable within the time frame of this study. Therefore, no evidence of accelerated basal melting has been observed.

6. Outlook

Several steps can be taken to further advance the topics addressed in this study. These actions are briefly outlined below.

A key issue that has emerged is the variability of the 3S value and questions regarding the measurement accuracy of the instruments used. The 3S value has a significant impact on the calculated GMW fractions, and therefore, it should be as precise and realistic as possible. It would be interesting to determine over what distance significant changes in the 3S value occur and how large these changes might be. For instance, would samples taken from the ice shelf front differ significantly from those taken near the continental slope or beyond? The data analyzed here suggests that samples must be taken continuously, ideally annually, to capture short-term variability for such an assessment. Additionally, different institutions should collect and analyze identical surface samples to rule out instrument-related or calibration-related issues. However, the latter could present a challenge, as such investigations require specific setups available only at a few specialized institutes worldwide.

Regardless of the GMW fractions, accurately determining the 3S value and its variability is essential if noble gases are to be used to compute sea ice production. Even though the assumptions used in this study are simplified, they have shown a realistic magnitude of the estimates. While satellite data is currently the main tool for estimating sea ice formation, noble gas studies could potentially support this in the future. It would be necessary to refine the applied methods, improve the assumptions made, and better integrate the results with those of other studies.

Further valuable investigations could focus on wind patterns. The wind is one of the main driving forces behind sea ice formation, circulation beneath the FRIS, and basal melting. It also strongly influences air-sea interactions and, thus, the 3S values, which are crucial for GMW calculations. A detailed analysis of wind patterns over several years, both locally in the Weddell Sea and on a larger scale, as across Antarctica and the Southern Ocean, could reveal important correlations. Such studies would connect several elements: the variability of the 3S value, sea ice formation, circulation beneath the FRIS, and the resulting meltwater fractions.

7. References

Akhoudas, C., Sallée, J., Reverdin, G., Aloisi, G., Benetti, M., Vignes, L., Gelado, M., 2020. Ice Shelf Basal Melt and Influence on Dense Water Outflow in the Southern Weddell Sea. JGR Oceans 125, e2019JC015710. https://doi.org/10.1029/2019JC015710

Bamber, J.L., Riva, R.E.M., Vermeersen, B.L.A., LeBrocq, A.M., 2009. Reassessment of the Potential Sea-Level Rise from a Collapse of the West Antarctic Ice Sheet. Science 324, 901–903. https://doi.org/10.1126/science.1169335

Berghald, M. 2021. Rekonstruktion und Variabilität des Schmelzwassereintrags vom Filchner-Ronne-Schelfeis mittels Messungen von Helium- und Neon. Projektarbeit.

Bieri, R., Koide, M., & Goldberg, E. D. (1964). Noble gases in sea water. Science, 146(3647), 1035–1037. https://doi.org/10.1126/science.146.3647.1035

Center for Coastal Physical Oceanography, Old Dominion University, Dinniman, M., Asay-Davis, X., Galton-Fenzi, B., Holland, P., Jenkins, A., Timmermann, R., 2016. Modeling Ice Shelf/Ocean Interaction in Antarctica: A Review. Oceanog. 29, 144–153. https://doi.org/10.5670/oceanog.2016.106

Corr, H.F.J., Jenkins, A., Nicholls, K.W., Doake, C.S.M., 2002. Precise measurement of changes in ice-shelf thickness by phase-sensitive radar to determine basal melt rates: ICE MELT RATES REVEALED BY RADAR. Geophys. Res. Lett. 29, 73-1-74–4. https://doi.org/10.1029/2001GL014618

Craig, H., & Scarsi, P. (1997). Helium isotope stratigraphy in the GISP2 ice core. *Eos, Transactions American Geophysical Union*, *78*(7).

Daae, K., Hattermann, T., Darelius, E., Mueller, R.D., Naughten, K.A., Timmermann, R., Hellmer, H.H., 2020. Necessary Conditions for Warm Inflow Toward the Filchner Ice Shelf, Weddell Sea. Geophysical Research Letters 47, e2020GL089237. https://doi.org/10.1029/2020GL089237

Darelius, E., Fer, I., Nicholls, K.W., 2016. Observed vulnerability of Filchner-Ronne Ice Shelf to wind-driven inflow of warm deep water. Nat Commun 7, 12300. https://doi.org/10.1038/ncomms12300

Deike, L., Melville, W.K., 2018. Gas Transfer by Breaking Waves. Geophysical Research Letters 45. https://doi.org/10.1029/2018GL078758

Dorschel, B., Hehemann, L., Viquerat, S., Warnke, F., Dreutter, S., Schulze Tenberge, Y., Accettella, D., An, L., Barrios, F., Bazhenova, E.A., Black, J., Bohoyo, F., Davey, C., de Santis, L., Escutia Dotti, C., Frémand, A.C., Fretwell, P.T., Gales, J.A., Gao, J., Gasperini, L., Greenbaum, J.S., Henderson Jencks, J., Hogan, K.A., Hong, J.K., Jakobsson, M., Jensen, L., Kool, J., Larin, S., Larter, R.D., Leitchenkov, G.L., Loubrieu, B., Mackay, K., Mayer, L., Millan, R., Morlighem, M., Navidad, F., Nitsche, F.-O., Nogi, Y., Pertuisot, C., Post, A.L., Pritchard, H.D., Purser, A., Rebesco, M., Rignot, E., Roberts, J.L., Rovere, M., Ryzhov, I., Sauli, C., Schmitt, T., Silvano, A., Smith, J.E., Snaith, H., Tate, A.J., Tinto, K., Vandenbossche, P., Weatherall, P., Wintersteller, P., Yang, C., Zhang, T., Arndt, J.E., 2022. The International Bathymetric Chart of the Southern Ocean Version 2 (IBCSO v2). https://doi.org/10.1594/PANGAEA.937574

Drucker, R., Martin, S., and Kwok, R.: Sea ice production and export from coastal polynyas in the Weddell and Ross Seas, Geophys. Res. Lett., 38, https://doi.org/10.1029/2011GL048668, 2011.

Foldvik, A., GAMMELSRøD, T., TøRRESEN, T., 1985. Hydrographic observations from the Weddell Sea during the Norwegian Antarctic Research Expedition 1976/77. Polar Research 3, 177–193. https://doi.org/10.1111/j.1751-8369.1985.tb00506.x

Foldvik, A., Gammelsrød, T., Nygaard, E., Østerhus, S., 2001. Current measurements near Ronne Ice Shelf: Implications for circulation and melting. J. Geophys. Res. 106, 4463–4477. https://doi.org/10.1029/2000JC000217

Foster, T.D., Carmack, E.C., 1976. Frontal zone mixing and Antarctic Bottom water formation in the southern Weddell Sea. Deep Sea Research and Oceanographic Abstracts 23, 301–317. https://doi.org/10.1016/0011-7471(76)90872-X

Fox, A.J., Paul, A., Cooper, R., 1994. Measured properties of the Antarctic ice sheet derived from the SCAR Antarctic digital database. Polar Record 30, 201–206. https://doi.org/10.1017/S0032247400024268

Fretwell, P., Pritchard, H.D., Vaughan, D.G., Bamber, J.L., Barrand, N.E., Bell, R., Bianchi, C., Bingham, R.G., Blankenship, D.D., Casassa, G., Catania, G., Callens, D., Conway, H., Cook, A.J., Corr, H.F.J., Damaske, D., Damm, V., Ferraccioli, F., Forsberg, R., Fujita, S., Gim, Y., Gogineni, P., Griggs, J.A., Hindmarsh, R.C.A., Holmlund, P., Holt, J.W., Jacobel, R.W., Jenkins, A., Jokat, W., Jordan, T., King, E.C., Kohler, J., Krabill, W., Riger-Kusk, M., Langley, K.A., Leitchenkov, G., Leuschen, C., Luyendyk, B.P., Matsuoka, K., Mouginot, J., Nitsche, F.O., Nogi, Y., Nost, O.A., Popov, S.V., Rignot, E., Rippin, D.M., Rivera, A., Roberts, J., Ross, N., Siegert, M.J., Smith, A.M., Steinhage, D., Studinger, M., Sun, B., Tinto, B.K., Welch, B.C., Wilson, D., Young, D.A., Xiangbin, C., Zirizzotti, A., 2013. Bedmap2: improved ice bed, surface and thickness datasets for Antarctica. The Cryosphere 7, 375–393. https://doi.org/10.5194/tc-7-375-2013

Gammelsrød, T., Foldvik, A., Nøst, O. A., Foldvik, Ø., Anderson, L. G., Fogelqvist, E., et al. (1994). Distribution of water masses on the continental shelf in the southern Weddell Sea. In The polar oceans and their role in shaping the global environment (pp. 159–176).

American Geophysical Union (AGU). https://doi.org/10.1029/GM085p0159Gardner, A.S., Moholdt, G., Scambos, T., Fahnstock, M., Ligtenberg, S., Van Den Broeke, M., Nilsson, J., 2018. Increased West Antarctic and unchanged East Antarctic ice discharge over the last 7 years. The Cryosphere 12, 521–547. https://doi.org/10.5194/tc-12-521-2018

Gill, A.E., 1973. Circulation and bottom water production in the Weddell Sea. Deep Sea Research and Oceanographic Abstracts 20, 111–140. https://doi.org/10.1016/0011-7471(73)90048-X

Hahm, D., Postlethwaite, C.F., Tamaki, K., Kim, K.-R., 2004. Mechanisms controlling the distribution of helium and neon in the Arctic seas: the case of the Knipovich Ridge. Earth and Planetary Science Letters 229, 125–139. https://doi.org/10.1016/j.epsl.2004.10.028

Haid, V. and Timmermann, R.: Simulated heat flux and sea ice production at coastal polynyas in the southwestern Weddell Sea, J. Geophys. Res.-Oceans, 118, 2640–2652, https://doi.org/10.1002/jgrc.20133, 2013.

Hattermann, T., Nicholls, K.W., Hellmer, H.H., Davis, P.E.D., Janout, M.A., Østerhus, S., Schlosser, E., Rohardt, G., Kanzow, T., 2021. Observed interannual changes beneath Filchner-Ronne Ice Shelf linked to large-scale atmospheric circulation. Nat Commun 12, 2961. https://doi.org/10.1038/s41467-021-23131-x

Hellmer, H.H., 2004. Impact of Antarctic ice shelf basal melting on sea ice and deep ocean properties: ANTARCTIC ICE SHELF BASAL MELTING. Geophys. Res. Lett. 31, n/a-n/a. https://doi.org/10.1029/2004GL019506

Hellmer, H.H., Kauker, F., Timmermann, R., Determann, J., Rae, J., 2012. Twenty-first-century warming of a large Antarctic ice-shelf cavity by a redirected coastal current. Nature 485, 225–228. https://doi.org/10.1038/nature11064

Heinemann, G., Braun, M., Brey, T., Damaske, D., Melles, M., Rhein, M., Willmes, S. (Hrsg.), 2017: Polarforschungsagenda 2030 – Status und Perspektiven der deutschen Polarforschung. Statusbericht des Deutschen Nationalkomitees SCAR/IASC der DFG, 160 Seiten. Verlag: Universität Trier, ISBN 978-3-00-057243-2.

Hohmann, R., 2002. Excess helium and neon in the southeast Pacific: Tracers for glacial meltwater. J. Geophys. Res. 107, 3198. https://doi.org/10.1029/2000JC000378

Huhn, O., Hattermann, T., Davis, P.E.D., Dunker, E., Hellmer, H.H., Nicholls, K.W., Østerhus, S., Rhein, M., Schröder, M., Sültenfuß, J., 2018. Basal Melt and Freezing Rates From First Noble Gas Samples Beneath an Ice Shelf. Geophys. Res. Lett. 45, 8455–8461. https://doi.org/10.1029/2018GL079706

Huhn, O., Hellmer, H.H., Rhein, M., Rodehacke, C., Roether, W., Schodlok, M.P., Schröder, M., 2008. Evidence of deep- and bottom-water formation in the western Weddell Sea. Deep Sea Research Part II: Topical Studies in Oceanography 55, 1098–1116. https://doi.org/10.1016/j.dsr2.2007.12.015

Huhn, O., Rhein, M., Bulsiewicz, K., Sültenfuß, J., 2021a. Noble gas (He, Ne isotopes) and transient tracer (CFC-12, SF6) measurements from POLARSTERN cruise PS111 (Weddell Sea, 2018). https://doi.org/10.1594/PANGAEA.930718

Huhn, O., Rhein, M., Kanzow, T., Schaffer, J., Sültenfuß, J., 2021b. Submarine Meltwater From Nioghalvfjerdsbræ (79 North Glacier), Northeast Greenland. J. Geophys. Res. Oceans 126. https://doi.org/10.1029/2021JC017224

Huhn, O., Rhein, M., Schröder, M., Bulsiewicz, K., Sültenfuß, J., 2017. CFC, and noble gas measurements during POLARSTERN cruise PS82 (ANT-XXIX/9). https://doi.org/10.1594/PANGAEA.883799

Intergovernmental Panel On Climate Change (Ipcc) (Ed.), 2023. Climate Change 2022 - Mitigation of Climate Change: Working Group III Contribution to the Sixth Assessment Report of the Intergovernmental Panel on Climate Change, 1st ed. Cambridge University Press. https://doi.org/10.1017/9781009157926

Jacobs, S.S., Jenkins, A., Giulivi, C.F., Dutrieux, P., 2011. Stronger ocean circulation and increased melting under Pine Island Glacier ice shelf. Nature Geosci 4, 519–523. https://doi.org/10.1038/ngeo1188

Janout, M.A., Hellmer, H.H., Hattermann, T., Huhn, O., Sültenfuss, J., Østerhus, S., Stulic, L., Ryan, S., Schröder, M., Kanzow, T., 2021. FRIS Revisited in 2018: On the Circulation and Water Masses at the Filchner and Ronne Ice Shelves in the Southern Weddell Sea. JGR Oceans 126. https://doi.org/10.1029/2021JC017269

Janout, M.A., Hellmer, H.H., Schröder, M., Wisotzki, A., 2019. Physical oceanography during POLARSTERN cruise PS111 (ANT-XXXIII/2). https://doi.org/10.1594/PANGAEA.897280

Jean-Baptiste, P., Petit, J.-R., Lipenkov, V.Ya., Raynaud, D., Barkov, N.I., 2001. Constraints on hydrothermal processes and water exchange in Lake Vostok from helium isotopes. Nature 411, 460–462. https://doi.org/10.1038/35078045

Kanwisher, J., 1963. On the exchange of gases between the atmosphere and the sea. Deep Sea Research and Oceanographic Abstracts 10, 195–207. https://doi.org/10.1016/0011-7471(63)90356-5

Loose, B., Jenkins, W.J., 2014. The five stable noble gases are sensitive unambiguous tracers of glacial meltwater: LOOSE AND JENKINS; NOBLE GASES ARE TRACERS OF MELTWATER. Geophys. Res. Lett. 41, 2835–2841. https://doi.org/10.1002/2013GL058804

Matsuoka, K., Hindmarsh, R.C.A., Moholdt, G., Bentley, M.J., Pritchard, H.D., Brown, J., Conway, H., Drews, R., Durand, G., Goldberg, D., Hattermann, T., Kingslake, J., Lenaerts, J.T.M., Martín, C., Mulvaney, R., Nicholls, K.W., Pattyn, F., Ross, N., Scambos, T., Whitehouse, P.L., 2015. Antarctic ice rises and rumples: Their properties and significance for ice-sheet dynamics and evolution. Earth-Science Reviews 150, 724–745. https://doi.org/10.1016/j.earscirev.2015.09.004

Matsuoka, K., Skoglund, A., Roth, G., De Pomereu, J., Griffiths, H., Headland, R., Herried, B., Katsumata, K., Le Brocq, A., Licht, K., Morgan, F., Neff, P.D., Ritz, C., Scheinert, M., Tamura, T., Van De Putte, A., Van Den Broeke, M., Von Deschwanden, A., Deschamps-Berger, C., Van Liefferinge, B., Tronstad, S., Melvær, Y., 2021. Quantarctica, an integrated mapping environment for Antarctica, the Southern Ocean, and sub-Antarctic islands. Environmental Modelling & Software 140, 105015. https://doi.org/10.1016/j.envsoft.2021.105015

Meredith, M.P., 2013. Replenishing the abyss. Nature Geosci 6, 166–167. https://doi.org/10.1038/ngeo1743

Nicholls, K.W., 2004. Interannual variability and ventilation timescales in the ocean cavity beneath Filchner-Ronne Ice Shelf, Antarctica. J. Geophys. Res. 109, C04014. https://doi.org/10.1029/2003JC002149

Nicholls, K.W., Abrahamsen, E.P., Buck, J.J.H., Dodd, P.A., Goldblatt, C., Griffiths, G., Heywood, K.J., Hughes, N.E., Kaletzky, A., Lane-Serff, G.F., McPhail, S.D., Millard, N.W., Oliver, K.I.C., Perrett, J., Price, M.R., Pudsey, C.J., Saw, K., Stansfield, K., Stott, M.J., Wadhams, P., Webb, A.T., Wilkinson, J.P., 2006. Measurements beneath an Antarctic ice shelf using an autonomous underwater vehicle. Geophys. Res. Lett. 33, L08612. https://doi.org/10.1029/2006GL025998

Nicholls, K.W., Østerhus, S., 2004. Interannual variability and ventilation timescales in the ocean cavity beneath Filchner-Ronne Ice Shelf, Antarctica. J. Geophys. Res. 109, 2003JC002149. https://doi.org/10.1029/2003JC002149

Nicholls, K. W., & Makinson, K. (1998). Ocean Circulation Beneath the Western Ronne Ice Shelf, as Derived from in Situ Measurements of Water Currents and Properties. In S. S. Jacobs & R. F. Weiss (Eds.), *Antarctic Research Series* (pp. 301–318). American Geophysical Union. https://doi.org/10.1029/AR075p0301

Nicholls, K.W., Østerhus, S., Makinson, K., Gammelsrød, T., Fahrbach, E., 2009. Ice-ocean processes over the continental shelf of the southern Weddell Sea, Antarctica: A review. Rev. Geophys. 47, RG3003. https://doi.org/10.1029/2007RG000250

Nicholls, K.W., Østerhus, S., Makinson, K., Johnson, M.R., 2001. Oceanographic conditions south of Berkner Island, beneath Filchner-Ronne Ice Shelf, Antarctica. J. Geophys. Res. 106, 11481–11492. https://doi.org/10.1029/2000JC000350

Nihashi, S. and Ohshima, K. I.: Circumpolar mapping of Antarctic coastal polynyas and landfast sea ice: Relationship and variability, J. Climate, 28, 3650–3670, https://doi.org/10.1175/JCLI-D- 14-00369.1, 2015a.

Nycander, J., Hieronymus, M., Roquet, F., 2015. The nonlinear equation of state of sea water and the global water mass distribution. Geophysical Research Letters 42, 7714–7721. https://doi.org/10.1002/2015GL065525

Oerter, H., Kipfstuhl, J., Determann, J. et al. Evidence for basal marine ice in the Filchner–Ronne ice shelf. Nature 358, 399–401 (1992). https://doi.org/10.1038/358399a0

Orsi, A.H., 2002. On the total input of Antarctic waters to the deep ocean: A preliminary estimate from chlorofluorocarbon measurements. J. Geophys. Res. 107, 3122. https://doi.org/10.1029/2001JC000976

Orsi, A.H., Johnson, G.C., Bullister, J.L., 1999. Circulation, mixing, and production of Antarctic Bottom Water. Progress in Oceanography 43, 55–109. https://doi.org/10.1016/S0079-6611(99)00004-X

Paolo, F.S., Fricker, H.A., Padman, L., 2015. Volume loss from Antarctic ice shelves is accelerating. Science 348, 327–331. https://doi.org/10.1126/science.aaa0940

Postlethwaite, C.F., Developing a tool for evaluating the role of seasonal sea ice in deep-water formation, PhD thesis, University of Southampton, 151 pp.

Paul, S., Willmes, S., Heinemann, G., 2015. Long-term coastal-polynya dynamics in the southern Weddell Sea from MODIS thermal-infrared imagery. The Cryosphere 9, 2027–2041. https://doi.org/10.5194/tc-9-2027-2015

Purich, A., Doddridge, E.W., 2023. Record low Antarctic sea ice coverage indicates a new sea ice state. Commun Earth Environ 4, 314. https://doi.org/10.1038/s43247-023-00961-9

Reese, R., Gudmundsson, G.H., Levermann, A., Winkelmann, R., 2018. The far reach of ice-shelf thinning in Antarctica. Nature Clim Change 8, 53–57. https://doi.org/10.1038/s41558-017-0020-x

Rhein, M., Steinfeldt, R., Huhn, O., Sültenfuß, J., Breckenfelder, T., 2018. Greenland Submarine Melt Water Observed in the Labrador and Irminger Sea. Geophysical Research Letters 45. https://doi.org/10.1029/2018GL079110

Rignot, E., Jacobs, S., Mouginot, J., Scheuchl, B., 2013. Ice-Shelf Melting Around Antarctica. Science 341, 266–270. https://doi.org/10.1126/science.1235798

Rignot, E., Mouginot, J., Scheuchl, B., Van Den Broeke, M., Van Wessem, M.J., Morlighem, M., 2019a. Four decades of Antarctic Ice Sheet mass balance from 1979–2017. Proc. Natl. Acad. Sci. U.S.A. 116, 1095–1103. https://doi.org/10.1073/pnas.1812883116

Rignot, E., Mouginot, J., Scheuchl, B., Van Den Broeke, M., Van Wessem, M.J., Morlighem, M., 2019b. Four decades of Antarctic Ice Sheet mass balance from 1979–2017. Proc. Natl. Acad. Sci. U.S.A. 116, 1095–1103. https://doi.org/10.1073/pnas.1812883116

Roether, W., Huhn, O., 2017. Chlorofluorocarbons, Noble Gases and Tritium measurements during POLARSTERN cruise ANT-XXII/3 - Filchner-Ronne Ice Shelf. https://doi.org/10.1594/PANGAEA.883832

Rosier, S.H.R., Hofstede, C., Brisbourne, A.M., Hattermann, T., Nicholls, K.W., Davis, P.E.D., Anker, P.G.D., Hillenbrand, C. -D., Smith, A.M., Corr, H.F.J., 2018. A New Bathymetry for the Southeastern Filchner-Ronne Ice Shelf: Implications for Modern Oceanographic Processes and

Glacial History. J. Geophys. Res. Oceans 123, 4610–4623. https://doi.org/10.1029/2018JC013982

Ryan, S., Hellmer, H.H., Janout, M., Darelius, E., Vignes, L., Schröder, M., 2020. Exceptionally Warm and Prolonged Flow of Warm Deep Water Toward the Filchner-Ronne Ice Shelf in 2017. Geophysical Research Letters 47, e2020GL088119. https://doi.org/10.1029/2020GL088119

Ryan, S., Schröder, M., Huhn, O., Timmermann, R., 2016. On the warm inflow at the eastern boundary of the Weddell Gyre. Deep Sea Research Part I: Oceanographic Research Papers 107, 70–81. https://doi.org/10.1016/j.dsr.2015.11.002

Schlosser, P., 1986. Helium: a new tracer in Antarctic oceanography. Nature 321, 233–235. https://doi.org/10.1038/321233a0

Schodlok, M.P., Menemenlis, D., Rignot, E.J., 2016. Ice shelf basal melt rates around Antarctica from simulations and observations: ICE SHELF BASAL MELT AROUND ANTARCTICA. J. Geophys. Res. Oceans 121, 1085–1109. https://doi.org/10.1002/2015JC011117

Schröder, M., 2010. Physical oceanography during POLARSTERN cruise ANT-XII/3. https://doi.org/10.1594/PANGAEA.742581

Schröder, M., Ryan, S., Wisotzki, A., 2016. Physical oceanography during POLARSTERN cruise PS96 (ANT-XXXI/2 FROSN). https://doi.org/10.1594/PANGAEA.859040

Schröder, M., Wisotzki, A., 2014. Physical oceanography during POLARSTERN cruise PS82 (ANT-XXIX/9). https://doi.org/10.1594/PANGAEA.833299

Shaw, W.J., Berg, L.K., Debnath, M., Deskos, G., Draxl, C., Ghate, V.P., Hasager, C.B., Kotamarthi, R., Mirocha, J.D., Muradyan, P., Pringle, W.J., Turner, D.D., Wilczak, J.M., 2022. Scientific challenges to characterizing the wind resource in the marine atmospheric boundary layer. Wind Energ. Sci. 7, 2307–2334. https://doi.org/10.5194/wes-7-2307-2022

Shepherd, A., Ivins, E.R., A, G., Barletta, V.R., Bentley, M.J., Bettadpur, S., Briggs, K.H., Bromwich, D.H., Forsberg, R., Galin, N., Horwath, M., Jacobs, S., Joughin, I., King, M.A., Lenaerts, J.T.M., Li, J., Ligtenberg, S.R.M., Luckman, A., Luthcke, S.B., McMillan, M., Meister, R., Milne, G., Mouginot, J., Muir, A., Nicolas, J.P., Paden, J., Payne, A.J., Pritchard, H., Rignot, E., Rott, H., Sørensen, L.S., Scambos, T.A., Scheuchl, B., Schrama, E.J.O., Smith, B., Sundal, A.V., Van Angelen, J.H., Van De Berg, W.J., Van Den Broeke, M.R., Vaughan, D.G., Velicogna, I., Wahr, J., Whitehouse, P.L., Wingham, D.J., Yi, D., Young, D., Zwally, H.J., 2012. A Reconciled Estimate of Ice-Sheet Mass Balance. Science 338, 1183–1189. https://doi.org/10.1126/science.1228102

Stulic, L., Timmermann, R., Paul, S., Zentek, R., Heinemann, G., Kanzow, T., 2023. Southern Weddell Sea surface freshwater flux modulated by icescape and atmospheric forcing. Ocean Sci. 19, 1791–1808. https://doi.org/10.5194/os-19-1791-2023

Suess, H. E., & Wänke, H. (1963). On the possibility of a helium flux through the ocean floor. Progress in Oceanography, 3, 347–353. https://doi.org/10.1016/0079-6611(65)90030-3

Sültenfuß, J., Roether, W., Rhein, M., 2009. The Bremen mass spectrometric facility for the measurement of helium isotopes, neon, and tritium in water. Isotopes in Environmental and Health Studies 45, 83–95. https://doi.org/10.1080/10256010902871929

The IMBIE team, 2018. Mass balance of the Antarctic Ice Sheet from 1992 to 2017. Nature 558, 219–222. https://doi.org/10.1038/s41586-018-0179-y

Timmermann, R., Hellmer, H.H., 2013. Southern Ocean warming and increased ice shelf basal melting in the twenty-first and twenty-second centuries based on coupled ice-ocean finite-element modelling. Ocean Dynamics 63, 1011–1026. https://doi.org/10.1007/s10236-013-0642-0

Tippenhauer, S., Janout, M.A., Schall, E., Timmermann, R., van Caspel, M., Vignes, L., Hinse, Y., Hellmer, H.H., 2023. Physical oceanography measured on water bottle samples based on ship CTD during RV POLARSTERN cruise PS124. https://doi.org/10.1594/PANGAEA.961780

Weiss, R.F., 1971. Solubility of helium and neon in water and seawater. J. Chem. Eng. Data 16, 235–241. https://doi.org/10.1021/je60049a019

Woolf, D.K., 1997. Bubbles and their role in gas exchange, in: Liss, P.S., Duce, R.A. (Eds.), The Sea Surface and Global Change. Cambridge University Press, pp. 173–206. https://doi.org/10.1017/CBO9780511525025.007

8. Appendix

A.1 Statistical Tools

IQR test: The Interquartile Range (IQR) test identifies outliers by calculating the range between the first and third quartiles of a dataset and flagging values that fall outside 1.5 times this range below the first quartile or above the third quartile.

Cook's Distance test: Cook's Distance is a measure used in regression analysis to identify influential outliers by calculating how much the regression model's coefficients would change if each observation were excluded from the analysis.

A.2 Statement about the usage of AI

I used the free version of the software Grammarly to check my spelling and grammar. Even though Grammarly is in the first place a tool to correct grammatical and spelling mistakes, it is powered by AI. No text of this thesis was generated by Grammarly. However, Grammarly would give a visual indication if a sentence could be improved. Yet, this is only an indication and Grammarly does not generate text when these indications are checked. So, technically an AI was used, but it lacked the actual advantages of AI.